Revisiting the martensite/ferrite interface damage initiation mechanism

Liu, L.; Maresca, F.; Hoefnagels, J. P. M.; Vermeij, T.; Geers, M. G. D.; Kouznetsova, V. G.

Published in:
Acta Materialia

DOI:
10.1016/j.actamat.2020.116533

Publication date:
2021

Acta Materialia 205 (2021) 116533

Contents lists available at ScienceDirect

Acta Materialia

journal homepage: www.elsevier.com/locate/actamat

Revisiting the martensite/ferrite interface damage initiation mechanism: The key role of substructure boundary sliding

L. Liu[a,b], F. Maresca[c], J.P.M. Hoefnagels[a], T. Vermeij[a,b], M.G.D. Geers[a], V.G. Kouznetsova[a,*]

[a] Department of Mechanical Engineering, Eindhoven University of Technology, 5600 MB Eindhoven, The Netherlands
[b] Materials Innovation Institute (M2i), 2600 GA Delft, The Netherlands
[c] Engineering and Technology Institute Groningen, Faculty of Science and Engineering, University of Groningen, 9747 AG Groningen, The Netherlands

ARTICLE INFO

Article history:
Received 24 July 2020
Revised 15 November 2020
Accepted 27 November 2020
Available online 3 December 2020

Keywords:
Dual-phase steel
Martensite/ferrite interface
Damage initiation
Substructure boundary sliding
Microstructural morphology
Crystal plasticity

ABSTRACT

Martensite/ferrite (M/F) interface damage plays a critical role in controlling failure of dual-phase (DP) steels and is commonly understood to originate from the large phase contrast between martensite and ferrite. This however conflicts with a few, recent observations, showing that considerable M/F interface damage initiation is often accompanied by apparent martensite island plasticity and weak M/F strain partitioning. In fact, martensite has a complex hierarchical structure which induces a strongly heterogeneous and orientation-dependent plastic response. Depending on the local stress state, (lath) martensite is presumed to be hard to deform based on common understanding. However, when favourably oriented, substructure boundary sliding can be triggered at a resolved shear stress which is comparable to that of ferrite. Moreover, careful measurements of the M/F interface structure indicate the occurrence of sharp martensite wedges protruding into the ferrite and clear steps in correspondence with lath boundaries, constituting a jagged M/F interfacial morphology that may have a large effect on the M/F interface behaviour. By taking into account the substructure and morphology features, which are usually overlooked in the literature, this contribution re-examines the M/F interface damage initiation mechanism. A systematic study is performed, which accounts for different loading conditions, phase contrasts, residual stresses/strains resulting from the preceding martensitic phase transformation, as well as the possible M/F interfacial morphologies. Crystal plasticity simulations are conducted to include inter-lath retained austenite (RA) films enabling the substructure boundary sliding. The results show that the substructure boundary sliding, which is the most favourable plastic deformation mode of lath martensite, can trigger M/F interface damage and hence control the failure behaviour of DP steels. The present finding may change the way in which M/F interface damage initiation is understood as a critical failure mechanism in DP steels.

1. Introduction

Facilitated by the economically viable thermo-mechanical processing procedures, low alloying requirements and excellent mechanical properties, dual-phase (DP) steels consisting of a ferrite (F)/(lath) martensite (M) microstructure are nowadays among the most attractive advanced high strength steels (AHSS) for automotive applications [1]. The exploitation of DP steels has triggered intense efforts to further increase their strength and ductility. However, a strength/ductility trade-off exists, as shown by several attempts to optimize the strength of DP steels by e.g. increasing the martensite volume fraction [2], the carbon content [3], the martensite island connectivity [4] and by grain refinement [5], which often result in a ductility decrease. Hence, this trade-off acts as a critical constraint for further improvements of DP steels towards manufacturing of light-weight complex structural components.

In order to overcome this challenge, considerable efforts have been devoted to understand DP steel failure. Based on a broad review of experimental data, Tasan et al. [6] concluded that M/F interface damage (which, as discussed by Hoefnagels et al. [7], is often referred to as “decohesion”) is the dominant origin of DP steel failure in the case of low (10%) to moderate (50%) martensite volume fractions, which holds true for most widely used DP grades. Moreover, it has been found that the voids nucleated at the M/F interface can grow easily, due to the relatively limited mechanical constraints induced by the martensite islands [8,9]. These facts in-

* Corresponding author.
E-mail address: v.g.kouznetsova@tue.nl (V.G. Kouznetsova).

https://doi.org/10.1016/j.actamat.2020.116533

deed show the importance of counteracting the M/F interface damage, in order to improve the overall ductility of DP steels.

Commonly, martensite is regarded as a hard constituent that shows negligible plasticity when embedded in the much softer ferrite. As a result, M/F interface damage is usually considered to originate from the large phase contrast between the ferrite matrix and martensite islands, which act as hard barriers for the dislocation glide in the ferrite [10]. Upon mechanical loading, dislocations gradually accumulate along the M/F interface, leading to a locally high stored energy. After reaching a certain threshold, the stored energy is released [11,12], eventually inducing void nucleation along the M/F interface [13].

This understanding of the M/F interface damage initiation mechanism is in qualitative agreement with many observations and thus is broadly accepted. For example, Das et al. [14] and Kadkhodapour et al. [15] reported that M/F interface damage was triggered preferentially around fine martensite islands (especially at their sharp ends) compared with the coarse martensite islands. This observation was correlated with the large curvature of the fine martensite islands, which, assuming a large M/F phase contrast, could induce large plastic strain localization and stress concentrations in the surrounding ferrite matrix. Additionally, Avramovic-Cingara et al. [16], Saeidi et al. [13] and Archie et al. [17] pointed out that M/F interface damage was mostly triggered at M/F/F triple junctions or where the martensite islands were closely spaced. The underlying mechanism causing damage could be plastic strain localization in the ferrite matrix in these regions, again relying on a large M/F phase contrast. Numerical simulations have also been performed testing the high M/F phase contrast hypothesis, showing that the predictions of the M/F interface damage initiation spots agree qualitatively with the corresponding experimental observations [18–20].

More recent detailed measurements, however, show data that is not consistent with the above understanding based on the high M/F phase contrast assumption. For instance, microscopic digital image correlation (micro-DIC) results have revealed that in DP steels, the martensite islands can deform up to large plastic strains ($>$ 50%) with weak M/F strain partitioning, even during the early deformation stages [21–26], which contradict the large M/F phase contrast assumption. Additionally, Samei et al. [27] demonstrated that, upon mechanical loading, the dislocations around the fine martensite islands would pile up inside the ferrite matrix, rather than accumulating along the M/F interface. *This new set of evidences asks for a deeper understanding of the M/F interface damage initiation mechanism*.

It is well known that lath martensite has a complex hierarchical structure characterized by a large amount of internal subgrain/substructure boundaries [28–30]. Recent experiments have demonstrated that these boundaries not only strengthen lath martensite, but also enable plastic deformation via substructure boundary sliding, when locally subjected to simple shear [31,32]. Extensive TEM evidence of the presence of continuous nanoscale inter-lath retained austenite (RA) films at all lath boundaries (also at those belonging to the same variant) in low carbon and low alloy steels [33–35], including DP steels [36,37], has inspired the modelling work by Maresca et al. [38,39]. In this work, it was shown that the existence of inter-lath RA films on which the harder laths can easily slide, may explain the substructure boundary sliding. This mechanism hinges on the specific M/A crystallographic orientation relationship (OR) and the low slip resistance associated with slip in the face-centered-cubic (FCC) austenite, compared to the body-centered-cubic (BCC) laths, resulting in easy activation of plastic deformation carried by dislocation glide parallel to the M/A interface. This substructure boundary sliding mechanism, based on the presence of the RA films, can also be accommodated by the martensitic phase transformation of the RA films [40], which can occur upon mechanical loading. Despite the fact that direct in-situ observations of thin film austenite plastic deformation or austenite-to-martensite transformation accompanying the substructure boundary sliding have not yet been performed (due to the small scales and the complexity), the assumption that the substructure boundary sliding is governed by the RA films [38–40] is consistent with multiple observations, and therefore will be also explored in this contribution.

Since martensite islands in DP steels have relatively few variants such that the internal boundaries cross almost the whole islands [41], the mentioned substructure boundary sliding could be correlated with the large heterogeneous plastic deformation of martensite in DP steels, as shown with numerical simulations by Maresca et al. [42] and experimentally by Du et al. [43]. Consequently, the sliding mechanism of the martensite islands may well result in significant deformation of the near-interface ferrite matrix thus triggering M/F interface damage. In addition, although most modelling work considers a smooth M/F interfacial morphology, recent detailed observations have identified the formation of sharp martensite wedges [44,45], that may also affect the M/F interface damage behaviour. These substructural morphological features are commonly disregarded when attempting to rationalize the M/F interface damage initiation mechanism. Therefore, this work aims at addressing the following two questions:

- Can the substructure boundary sliding trigger M/F interface damage?
- How does the M/F interfacial morphology affect damage initiation?

In order to address these questions, numerical modelling of the M/F interface mechanical behaviour is carried out, which incorporates the main features of the martensite island substructure and the M/F interfacial morphology. To the best of the authors' knowledge, a detailed experimental study of the M/F interfacial morphology has not been carried out yet, hence, first, an experimental study of the M/F interface structure is carried out to verify the presence of a jagged M/F interfacial morphology. This experimental study also provides further confirmation of substructure boundary sliding in lath martensite. Next, M/F interfaces with different morphologies are considered and modelled, for compactness, as one martensite island embedded in a ferrite matrix. The martensite island is composed of a set of BCC laths belonging to a single variant, stacked along the thickness direction and separated by inter-lath FCC RA films that enable substructure boundary sliding. The crystalline nature and the mutual OR of the BCC laths and FCC RA films are properly accounted for in the model. The mechanical behaviour of the M/F interface is investigated under different loading conditions, phase contrasts and residual stresses/strains due to the prior phase transformation. This modelling aims at a systematic study of the potential effects from different important M/F interface structural features, rather than providing a direct comparison to a specific experimentally measured M/F interface structure, or a specific phase behaviour.

The paper is organized as follows. First, experimental evidence of the jagged M/F interfacial morphology is reported and discussed in Section 2. Next, in Section 3 the modelling methods for the M/F interface are presented, and the boundary conditions considered for the loading are detailed. The crystal plasticity simulation results of the M/F interface behaviour under different loading, phase contrast and residual stress/strain conditions, together with the corresponding damage initiation analyses and discussions, are then presented in Section 4. The paper ends with Section 5 which summarizes the main conclusions of this work.

2. Experimental evidence of the M/F interfacial morphology and indication of the transformation-induced substructure boundary sliding

To the best of the authors' knowledge, no systematic analysis of the M/F interfacial morphology has so far been presented in the literature, and hence the commonly adopted assumption is that the M/F interface has a smooth morphology. This assumption might however be an oversimplification of the actual small-scale M/F interfacial morphology, as argued in the following.

It is known that, as the martensitic phase transformation occurs in a constrained environment, the martensite will tend to form in the shape of thin plates/laths with sharp edges, in order to minimize the elastic strain energy. Such sharp martensite wedges have been observed in a few austenitic steels [44,45]. In this light, the assumption of a smooth M/F interface may be an oversimplification. It seems more likely that laths in martensite islands form sharp edges at the M/F interface, which entails a jagged interfacial morphology in DP steels.

Furthermore, as discussed before, the martensite islands may have the capability to deform by substructure boundary sliding. If sliding occurs, then it would be logical that this mechanism is already activated during quenching, when the martensitic phase transformation occurs, in order to relieve the large stresses accommodating the phase transformation shape change. This mechanism itself might also induce a jagged M/F interfacial morphology, as sketched in Fig. 1(a).

In order to test this hypothesis, M/F interfaces in a heat-treated DP600 steel grade (Fe-0.092C-1.68Mn-0.57Cr-0.24Si wt.%) have been characterized in detail by using Electron Channeling Contrast Imaging (ECCI). The specimen was first annealed for 10 minutes at 1000 °C, then water quenched, and subsequently inter-critically annealed for 30 min at 770 °C, followed by a final water quenching. After the heat treatment, careful mechanical polishing with colloidal silica was performed on the specimen, in order to obtain a high-quality surface. ECCI micrographs of two particular interfaces are shown in Fig. 1(b–c), which indeed reveal a jagged morphology. At the M/F interfaces, a series of laths (with boundaries highlighted by black lines), and clear steps (white arrows) at the lath boundaries can be observed, along with dislocation accumulation at/between the lath tips (red arrows). These observations are consistent with the above stated hypotheses, that a jagged M/F interface can be induced either directly, by the formation of sharp martensite wedges, or indirectly, by the substructure boundary sliding mechanism, that can already occur during the phase transformation.

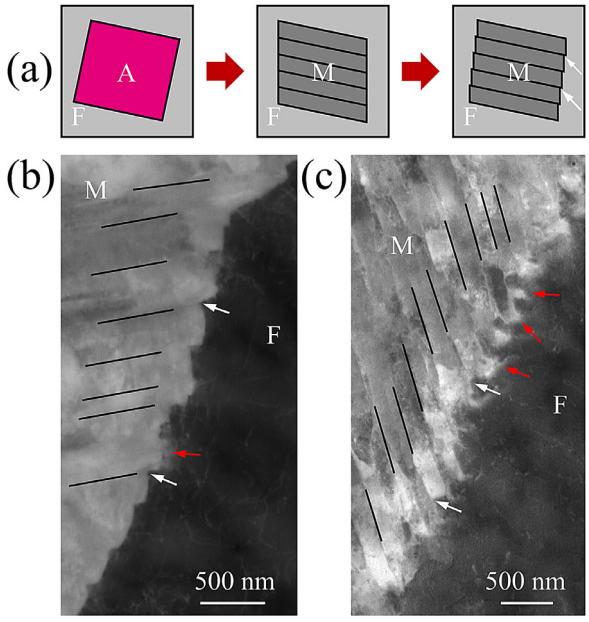

Fig. 1. (a) Schematic illustration of substructure boundary sliding that can potentially relieve the stresses in martensite, introduced by the overall shape change from the parent austenite grain to the product martensite island during the phase transformation; (b–c) ECCI micrographs of the jagged M/F interfaces in a DP steel specimen. Some lath boundaries are identified by black lines. White arrows highlight several clear steps, that occur in correspondence with the subgrain lath martensite boundaries and hence might be induced or enhanced by their sliding. Red arrows point to "plumes" within the near-interface ferrite matrix, which are indications of dislocation pile-ups due to the transformation-induced plasticity and the concurrent substructure boundary sliding in the martensite islands. (For interpretation of the references to colour in this figure legend, the reader is referred to the web version of this article.)

To the best of the authors' knowledge, this is the first time that a jagged M/F interfacial morphology has been clearly identified. There may be several possible reasons why this type of M/F interface formation has not been previously reported in the literature. First, a high-quality sample preparation, suited for ECCI, is required. Chemical and electro-chemical etching or polishing methods, regularly employed for the characterization of microstructures, while sufficient for distinguishing between the martensite and ferrite phases, easily affect the original M/F interface structure. Second, the high-resolution ECCI technique has not yet been employed with the specific aim of investigating the M/F interfacial morphology in DP steels. Moreover, attaining proper ECCI conditions is not a trivial task [46]. In general, the M/F interfacial morphology has not been identified before as a possibly important microstructural feature, which may explain why it has not received much attention in the literature. Finally, not all the M/F interfaces observed in this particular heat-treated DP grade exhibit a jagged morphology. One of the possible reasons is that the substructure boundary sliding, also in combination with the shape deformation, does not always occur in the imaging plane. Nevertheless, the result presented in Fig. 1 suggests that the mechanism of substructure boundary sliding can indeed be active in DP steels.

The main insights that emerge from this ECCI analysis, and that will guide the subsequent modelling approach, are:

- All steps occur at lath boundaries, suggesting that the substructure boundary sliding can indeed be active in the martensite islands during the martensitic phase transformation. The plastic deformation concentrates at the steps, which is a further mark of concurrent sliding induced by the phase transformation.
- This mark of sliding in combination with the martensitic phase transformation confirms indirect evidence in DP steels [43] and adds to the more extensive evidence in martensitic steels [31,32] of the substructure boundary sliding of lath martensite.
- Since the sliding seems to be activated already during the martensitic phase transformation, it is reasonable to presume that it will also be active upon subsequent mechanical loading, driven by the local shear stress state at the subgrain lath martensite boundaries. This hypothesis will be investigated systematically in the subsequent computational analyses.

3. Modelling methods

Based on the experimental evidence of substructure boundary sliding and the M/F interfacial morphology reported in Section 2, two main modelling hypotheses are made:

- RA films exist between the laths, governing the substructure boundary sliding.
- The M/F interfacial morphology can be either smooth or jagged after the phase transformation.

These two hypotheses, supported by experimental observations of the martensite island microstructure in the considered type of DP steel, will guide the choice of the modelling configurations and the material models.

3.1. Geometric model configurations

A commercial DP steel microstructure (Fe-0.092C-1.68Mn-0.57Cr-0.24Si wt.%) [47], highlighting a single martensite island embedded in the ferrite matrix is provided in Fig. 2(a). Due to the shared crystallographic orientation of the laths belonging to the same variant, the lath boundaries (red lines) in each sub-block are not visible in the Electron Backscatter Diffraction (EBSD) orientation map. Nevertheless, it is well-known that the sub-block in the DP steel martensite island consists of a set of laths. Lath boundaries share the same habit-plane as the (sub-)block boundaries (cyan lines) and are thus approximately parallel. Due to the relatively few variants in the DP steel martensite island, the substructure boundaries cross almost the whole island. As already widely evidenced in Section 1, laths can easily slide on these substructure boundaries and one experimental example from [31] is shown in Fig. 2(b), where the substructure boundary sliding is clearly visible in a full martensitic steel specimen (same alloying as in Fig. 2(a)) through a micro-tensile test. Note that the lath martensite in Fig. 2(b) originates from a larger prior austenite grain, compared to the martensite island in Fig. 2(a) and thus has a larger lath thickness, which also make the lath boundaries more visible.

For convenience of computational modelling, let us consider a DP steel microstructure simplified from Fig. 2(a), as sketched in Fig. 2(c). At this scale, the martensite island substructure and the M/F interfacial morphology are not resolved. By zooming on the martensite island, its detailed substructure is revealed: the martensite island consists of a set of BCC laths, stacked along the thickness direction, with FCC RA films in between. In order to model this substructure, a unit cell representing the M/F interface is constructed as indicated in Fig. 2(d). Each lath is approximately flat and elongated along the habit plane, as sketched in Fig. 2(e). Corresponding martensite island substructure and several possible M/F interfacial morphologies are shown in Fig. 2(f). In the model, a Kurdjumov-Sachs (K-S) OR is selected between the BCC laths and the FCC RA films, since all plausible OR models (such as Nishiyama-Wassermann and Greninger-Troiano) are approximations of the actual material and have limited differences (within few degrees) from each other. All laths are taken to belong to the same variant $(111)_\gamma \| (011)_{\alpha'}$, $[10\bar{1}]_\gamma \| [11\bar{1}]_{\alpha'}$, since it is known from the literature, e.g. [41], that for the considered type of DP steel, usually only a few (also see Fig. 2(a)) or just a single variant is present within one martensite island. Notice that the conclusions of this analysis will also hold true for all other symmetry-related K-S variants.

By assuming periodicity, the unit cell represents a locally infinite interface structure, which is a fair representation of the interface when the thickness of the laths is much smaller than the overall size of the martensite island (and corresponding (sub-)block), which is generally the case in DP steels (also see Fig. 2(a)). Note that the M/F interface of interest is far from the lateral boundaries of the computational unit cell, therefore, the numerical investigations are not restricted by the periodicity assumption along the horizontal direction. The global coordinate system is defined with respect to the habit plane $(111)_\gamma$, where X-axis, Y-axis and Z-axis denote, respectively, the length, thickness and width directions of the BCC lath, as shown in Fig. 2. The lath boundary planes are parallel to the habit plane and thus depicted to be parallel to the out-of-plane direction. Based on the fact that the lath width (in the out-of-plane direction, see Fig. 2(e)) is almost one order of magnitude larger than its thickness [29,30,48], a constant (extruded) out-of-plane microstructure is assumed. The simulations are therefore three-dimensional (3D) to properly account for the crystallography and slip systems. Without loss of generality for the considered type of DP steel, the martensite volume fraction in the unit cell is taken as 20%. The unit cell length is $L = 10$ μm and thickness is $T = 100$ nm, while the RA film thickness is $t_2 = 10$ nm, yielding a lath thickness $t_1 = 90$ nm and a lath length $l = 2$ μm - with small deviations from this value depending on the specific M/F interfacial morphology.

Aiming for a wide range, four possible M/F interfacial morphologies are considered, as shown in Fig. 2(f):

- "IM-1": sharp laths that partially penetrate through the prior austenite boundaries.
- "IM-2": sharp laths that fully penetrate through prior austenite boundaries.
- "IM-3": sharp laths that stop at prior austenite boundaries.
- "IM-4": blunted laths that stop at prior austenite boundaries.

For the configurations "IM-1", "IM-2" and "IM-3", a sharp lath tip angle 60° is adopted in order to magnify the potential influences of the M/F morphology, which can be jagged due to a transformation strain magnitude as high as 90% [49]. Notice that although RA volume fractions vary slightly among the different configurations, they are globally small, being all $\sim 2.5\%$ ("IM-1" 2.22%, "IM-2" 2.15%, "IM-3" 2.84% and "IM-4" 2.22%) and therefore the influence of such minute changes is preassumed to be negligible [38].

Simulations are performed using the finite element method (FEM). The geometry of each unit cell is discretized using 3D quadratic elements with one element in the out-of-plane direction. In order to balance the computational accuracy and cost, the finite element discretization is tailored, leading to a fine mesh near the M/F interface and coarse mesh far from the M/F interface, with averaged in-plane element sizes ~ 5 nm and ~ 25 nm, respectively (see Fig. 2(g)). A mesh sensitivity check has been carried out for all considered unit cell configurations, which has confirmed that both local and global responses are converged for the propsed discretizations. Periodic boundary conditions [50] are enforced along all directions in order to model the in-plane periodicity and constant microstructure in the out-of-plane direction.

3.2. Material models

3.2.1. Lath and retained austenite film

Since BCC and FCC crystals have a cubic symmetry, and the OR between austenite and martensite plays a key role, crystal plasticity modelling with cubic elasticity is employed for the constitutive description of the material behaviour of both BCC laths and FCC RA films. In addition to the crystal plasticity framework [51], the model is extended in order to take into account the effects of the preceding phase transformation, as briefly summarized below (see also Appendix A for more details).

In finite strains, the total deformation gradient tensor $\mathbf{F}$ is multiplicatively decomposed into the elastic ($\mathbf{F}_e$), phase transformation ($\mathbf{F}_{tr}$) and plastic ($\mathbf{F}_p$) parts as follows: $\mathbf{F} = \mathbf{F}_e \cdot \mathbf{F}_{tr} \cdot \mathbf{F}_p$. In this work, elasticity is described using a linear relation between $\tilde{\mathbf{S}}$ which is the push forward of the second Piola-Kirchhoff stress tensor $\mathbf{S}$ towards the second intermediate configuration, i.e., after applying $\mathbf{F}_p$ and $\mathbf{F}_{tr}$, and the elastic Green-Lagrangian strain tensor $\tilde{\mathbf{E}}_e$, as $\tilde{\mathbf{S}} = \mathbb{C} : \tilde{\mathbf{E}}_e$. The cubic elasticity tensor $\mathbb{C}$ is fully determined by specifying the three elasticity constants C_{11}, C_{12} and C_{44}. The deformation associated with the phase transformation is described by an invariant-plane strain, which depends on the transformation strain magnitude ε_{tr}, the habit plane normal $\vec{m}_{hp}$ and the transformation direction $\vec{s}_{tr}$ [49]. The plastic velocity gradient $\mathbf{L}_p = \dot{\mathbf{F}}_p \cdot \mathbf{F}_p^{-1}$

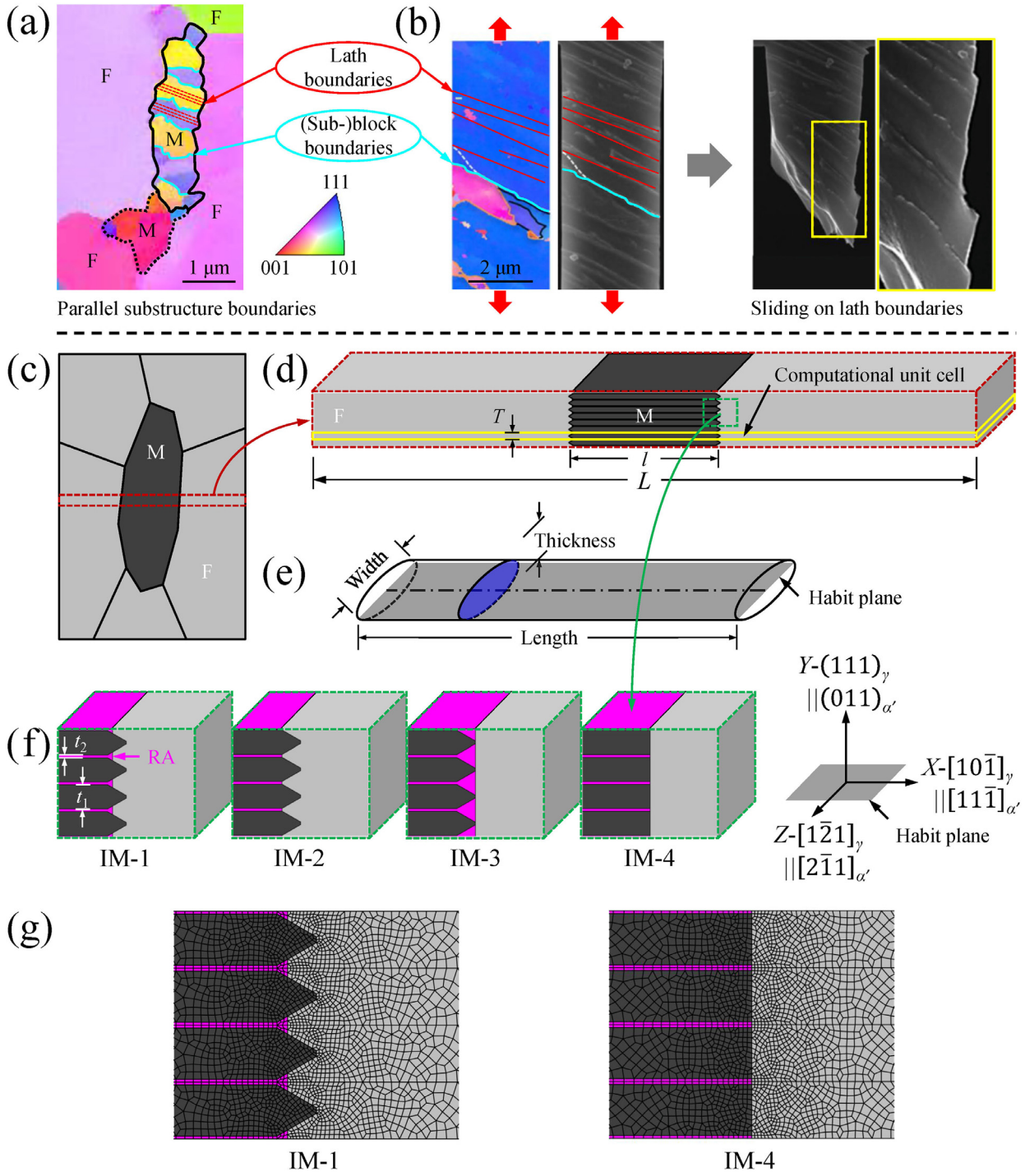

Fig. 2. (a) EBSD orientation map of a DP steel microstructure, focusing on a single martensite island, which contains only a few variants, thereby the substructure boundaries span the whole island. The lath boundaries are not visible, yet known to be parallel to the (sub-)block boundaries as they share the same habit-plane. The minor variants not belonging to the main packet are marked by black dotted lines. Reproduced from [47] with permission from Elsevier; (b) experimentally observed sliding activity on the lath boundaries in a full martensitic steel specimen (same alloying as in (a), but with coarser lath martensite) during the micro-tensile test, which is hypothesized to be governed by the inter-lath RA films. The tensile direction is denoted by red arrows. Reproduced from [31] with permission from Elsevier; (c) schematic illustration of one martensite island in which only one variant is assumed to exist, surrounded by the ferrite matrix; (d) magnification revealing the martensite island substructure, which is modelled within the computational unit cell, indicated by a yellow box; (e) sketch of a single lath, which is approximately flat and elongated along the habit plane. The lath cross-section along the length direction is highlighted in blue; (f) magnification of the M/F interfaces, showing four different possible M/F interfacial morphologies (IM); (g) in-plane finite element meshes around the M/F interfaces of two unit cell configurations. (For interpretation of the references to colour in this figure legend, the reader is referred to the web version of this article.)

Table 1
The material parameters of the BCC laths and the FCC RA films.

Parameter	Symbol	Lath	RA film
Elasticity component 11	C_{11}	349 [GPa]	268 [GPa]
Elasticity component 12	C_{12}	202 [GPa]	156 [GPa]
Elasticity component 44	C_{44}	176 [GPa]	136 [GPa]
Reference slip rate	$\dot{\gamma}_0$	0.01 [s^{-1}]	0.01 [s^{-1}]
Initial slip resistance	s_0	0.765 [GPa]	0.265 [GPa]
Saturation slip resistance	s_∞	3 [GPa]	0.34 [GPa]
Reference hardening modulus	h_0	2.25 [GPa]	0.25 [GPa]
Strain rate sensitivity	m	0.05 [−]	0.05 [−]
Hardening exponent	n	1.5 [-]	1.5 [-]
Latent/self hardening ratio	q	1.4 [-]	1.4 [-]
Slip family	$\{\vec{n}\}\langle\vec{s}\rangle$	$\{110\}_{\alpha'}\langle 111\rangle_{\alpha'}$ $\{112\}_{\alpha'}\langle 111\rangle_{\alpha'}$	$\{111\}_{\gamma}\langle 110\rangle_{\gamma}$

is computed as a function of the slip rate $\dot{\gamma}^\alpha$ and the Schmid tensor $\mathbf{P}_0^\alpha$ of each of the N_s slip systems as $\mathbf{L}_p = \sum_{\alpha=1}^{N_s} \dot{\gamma}^\alpha \mathbf{P}_0^\alpha$. The crystallographic slip of the αth slip system is driven by the resolved shear stress τ^α and computed by means of a power law [52]

$$\dot{\gamma}^\alpha = \dot{\gamma}_0^\alpha \left(\frac{|\tau^\alpha|}{s^\alpha} \right)^{\frac{1}{m}} \mathrm{sign}(\tau^\alpha), \tag{1}$$

where $\dot{\gamma}_0^\alpha$ denotes the initial slip rate, s^α the slip resistance and m the strain rate sensitivity. Notice that a sufficiently small value for m should be used to ensure a low rate dependence. In order to take hardening contributions [53] into account, s^α is evaluated using

$$\dot{s}^\alpha = \sum_{\beta=1}^{N_s} h^{\alpha\beta} |\dot{\gamma}^\beta|, \tag{2}$$

with the hardening modulus matrix element $h^{\alpha\beta}$ given by

$$h^{\alpha\beta} = h_0 \left(1 - \frac{s^\alpha}{s_\infty} \right)^n [q + (1-q)\delta^{\alpha\beta}], \tag{3}$$

where h_0 denotes the initial hardening modulus, s_∞ the saturation slip resistance, n the hardening exponent, q the latent/self hardening modulus ratio; δ is the Kronecker delta.

The crystal plasticity model described above is implemented for numerical simulations using a user-defined subroutine HYPELA2.F, supported in the commercial FEM package MSC.MARC.

The material parameters for the BCC laths and the FCC RA films are listed in Table 1. These parameters are based on [39], where they were identified from micro-tensile experimental data reported in Mine et al. [54], for two fully martensitic micron-size specimens (gauge section: 20 µm × 20 µm× 50 µm), containing several martensitic variants with fully indexed crystallography. However, the martensite in Mine et al. [54] had a carbon content 0.13 wt.% C, while commercial DP steels, e.g. DP600 steel, typically has an overall carbon content 0.1 wt.% C; for the considered martensite volume fraction (20%), the average carbon content in the martensite island is then expected to be ∼ 0.4 wt.% C (due to the low carbon solubility of the ferrite). This implies a substantial increase in the martensite hardness [55], whereas the austenite hardness is known to be much less sensitive to the carbon content [56]. A few important material parameters of the BCC laths, namely the initial slip resistance, the saturation slip resistance and the reference hardening modulus, are scaled such that when the substructure boundary sliding is inactive, the computed overall mechanical response of the martensite island is comparable to the micropillar compression experimental data in Ghassemi-Armaki et al. [57], Tian et al. [58], where a yield stress ∼ 2–3 GPa, has been reported for DP steel martensite island with a carbon content ∼ 0.3–0.4 wt.% C and multiple variants. Indeed, multiplying the BCC lath initial slip resistance used here (0.765 GPa) by a Taylor factor of 2.73 [59] corresponds to the expected yield stress of a martensitic polycrystal in the order of ∼ 2 GPa.

Table 2
The material parameters of the ferrite matrix.

Parameter	Symbol	F matrix
Young's modulus	E	200 [GPa]
Poisson's ratio	ν	0.3 [−]
Initial yield stress	S_0	0.45 (0.25–0.55) [GPa]
Saturation yield stress	S_∞	0.678 (0.27–1) [GPa]
Characteristic strain	E_c	0.0351 [−]

3.2.2. Ferrite matrix

Like the BCC laths, the ferrite matrix consists of BCC crystals. Nevertheless, there is no clear evidence of a preferential crystal orientation of the ferrite with respect to the martensite islands in DP steels. To limit the model parameter variation space, isotropic elasto-plasticity is used to describe the behaviour of the ferrite, thus neglecting the ferrite grain orientation effects. This assumption is motivated by recent detailed experimental investigations [58], showing that ferrite in DP steels may activate any of the 48 active slip systems of the {110}, {112} and {123} families, each activating at comparable stresses and following the Schmid's law. Furthermore, isotropic elasto-plasticity is an accurate approximation for a M/F phase contrast > 4 [60], which is the case in the present study. Moreover, compared to the hardening induced by the mechancial loading, the local preliminary hardening on the near-interface ferrite due to the interfacial misfit between martensite and ferrite constitutes a secondary effect [61], and is therefore not considered in the ferrite matrix modelling.

The constitutive law in the elastic regime follows the linear relation $\bar{\mathbf{S}} = \mathbb{C} : \bar{\mathbf{E}}_e$, where the isotropic elasticity tensor $\mathbb{C}$ is determined by Young's modulus E and Poisson's ratio ν. In the plastic regime, the von Mises yield condition is employed, in terms of the equivalent von Mises stress S^{eq} and the equivalent plastic strain rate $\dot{E}_p^{eq} = \sqrt{\frac{2}{3}\dot{\mathbf{E}}_p : \dot{\mathbf{E}}_p}$. An exponentially saturating hardening law is selected to account for the evolution of yield stress S_y up to a saturation yield stress S_∞ [62], reading

$$S_y = S_\infty - (S_\infty - S_0) \exp\left(-\frac{E_p^{eq}}{E_c} \right), \tag{4}$$

where S_0 denotes the initial yield stress, E_c the characteristic strain and $E_p^{eq} = \int \dot{E}_p^{eq}\, dt$ the (accumulated) equivalent plastic strain.

The material parameters for the ferrite matrix model listed in Table 2 were identified by fitting the experimental stress-strain data for the ferrite matrix from the uniaxial tensile tests, for a transformation-induced plasticity (TRIP) steel specimen with an overall carbon content ∼ 0.3 wt.% C, reported by Lani et al. [63], where the phase specific stress-strain responses were obtained from neutron diffraction measurements. Based on a broad range of tensile test data for different ferritic steel grades, realistic ranges of the yield stress and the ratio of the yield stress to the ultimate tensile strength for ferrite have been summarized by Tao and Rasmussen [64]. Since the ultimate tensile strength is often comparable to the saturation yield stress, realistic ranges of S_0 and S_∞ can be estimated; they are provided in Table 2 in parentheses, in order to support the subsequent phase contrast studies and sensitivity check of the numerical investigations with respect to the ferrite matrix parameters.

3.3. Loading conditions

Two mechanical loading conditions are considered, simple shear and biaxial loading, as sketched in Fig. 3. This choice is based

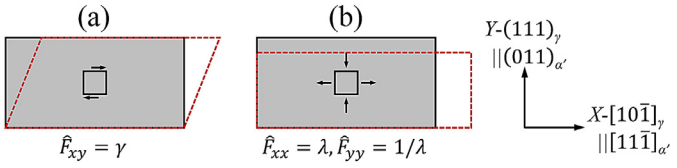

Fig. 3. Two mechanical loading conditions: (a) simple shear and (b) biaxial loading, together with the sketches of associated deformation states of a material element. The deformed configuration is denoted by a red box.

on previous work [38], where it was shown that the first loading condition can easily activate the substructure boundary sliding while the other cannot.

The simple shear is parameterized using the shear magnitude γ and the shear direction aligned with the habit plane, while the biaxial loading is parameterized using the stretch ratio λ and hence represents a case where the shear direction is tilted by 45° with respect to the habit plane. In order to minimize the external constraints and avoid an overestimation of damage initiation, overall plane stress boundary conditions are adopted. Consequently, the overall prescribed deformation gradients $\hat{\mathbf{F}}$ for the two loading conditions, simple shear and biaxial loading (marked by the superscripts "SS" and "BL", respectively) are given by

$$\hat{\mathbf{F}}^{\mathrm{SS}} = \begin{bmatrix} 1 & \gamma & \times \\ 0 & 1 & \times \\ 0 & 0 & \times \end{bmatrix}, \quad \hat{\mathbf{F}}^{\mathrm{BL}} = \begin{bmatrix} \lambda & 0 & \times \\ 0 & 1/\lambda & \times \\ 0 & 0 & \times \end{bmatrix}, \tag{5}$$

where "×" denotes the unprescribed (unknown) component.

To simulate the preceding phase transformation and the induced residual stress/strain fields, it is assumed that the lath is generated instantly such that $\mathbf{F}_{\mathrm{tr}}$ can be directly prescribed on the whole lath. Consistent with the simplified model geometry, the habit plane is approximated by $\vec{n}_{\mathrm{hp}} = (1,1,1)_\gamma$, which is 10° from the actual habit plane, and the transformation direction $\vec{s}_{\mathrm{tr}} = [0.8075, -0.1614, -0.5673]_\gamma$ is taken from [40], while the transformation strain magnitude $\varepsilon_{\mathrm{tr}}$ is varied in order to study the effect of different shape deformation magnitudes on the M/F interface damage initiation. For the transformation simulation, the overall stress free boundary conditions are adopted to minimize external constraints. Note, however, that as a result of the shape and volume change inside the martensite island, the stresses inside all phases are non-zero but are self-equilibrating in accordance with the zero external force.

4. Results and discussion

4.1. Influence of the loading conditions

In this part, the residual stress/strain effects are not yet considered, and hence $\mathbf{F}_{\mathrm{tr}} = \mathbf{I}$. Under different mechanical loading conditions, the overall response of each unit cell configuration and the overall sliding magnitude $||\vec{\gamma}_{\mathrm{hp}}||$ of the martensite island are shown in Fig. 4. To understand the individual phase behaviour, the overall responses of the martensite island (M/A laminate) and the ferrite matrix are also provided in Fig. 4(a) and (c). Here $\boldsymbol{\sigma}$ denotes the Cauchy stress, $\boldsymbol{\varepsilon}$ the logarithmic strain, $(\hat{\bullet})$ the volume average of a quantity over the whole unit cell domain, the martensite island domain or the ferrite matrix domain, as specified on the graphs. The overall sliding of the martensite island $\vec{\gamma}_{\mathrm{hp}}$ is defined by the effective shear deformation component of the M/A laminate along the habit plane (see Appendix B for more details), used to quantify the substructure boundary sliding activity. For all M/F interfacial morphologies, apparent martensite island plasticity is observed under both loading conditions, as seen in Fig. 4(a) and (c). As expected, a much lower stress level is needed to deform the martensite island for the simple shear case, namely ~ 1/3 of the stress for the biaxial loading case, leading to much easier sliding activation of the martensite island, as reported in Fig. 4(b). Instead, as shown in Fig. 4(d), the sliding of the martensite island in the biaxial loading case is negligible. Note that the stress levels in the ferrite matrix are comparable for the two different loading cases. As a result, the overall stress level of the unit cell in the simple shear case is relatively low compared to the biaxial loading case. Moreover, the M/F interfacial morphology only slightly influences the martensite island's overall response and sliding, and therefore has a negligible impact on the unit cell overall response. The variations are mainly due to the small differences in RA volume fractions among the four unit cell configurations, of which "IM-3" has the highest value, yielding the lowest overall response and highest sliding magnitude of the martensite island.

In order to rationalize the above observations, the equivalent plastic strain maps of the four unit cells are shown in Fig. 5. For each M/F interfacial morphology, substructure boundary sliding is highly active in the simple shear case, while the lath itself remains nearly rigid. This is reflected in the overall response and sliding magnitude of the martensite island in Fig. 4(a–b), where the low effective flow stress is due to the martensite island sliding, which in turn, is accommodated by large plastic slip activity (> 60%) in RA films, as observed in Fig. 5(a). The substructure boundary sliding forces the near-interface ferrite matrix to deform significantly, leading to high plastic deformation localization (> 30%) around the RA film tips (see insets in Fig. 5(a)) and towards the ferrite matrix. For the ferrite matrix surrounding the lath tips, no pronounced plasticity can be identified. On the other hand, at the RA film tips, large plastic strain gradients can be found towards the near-interface ferrite matrix. This can physically be correlated with dislocation accumulation around the martensite islands, which is in adequate agreement with the experimental observations by Samei et al. [27]. In addition, RA blocks between the lath tips can relieve the plastic deformation localization in the near-interface ferrite matrix (see the plastic strain maps of the unit cell configurations "IM-1" and "IM-3" in Fig. 5(a)). Clearly, the whole plastic deformation pattern is governed by the interaction between the RA films and the ferrite matrix, while the M/F interfacial morphology only has a secondary effect. The jagged M/F interfacial morphology induces a plastic strain intensity in the near-interface ferrite matrix comparable to that with the smooth morphology (see the plastic strain maps of the unit cell configurations "IM-2" and "IM-4" in Fig. 5(a)), i.e. the morphology effects are relatively weak.

In the biaxial loading case, the substructure boundary sliding is almost inactive and the deformation of the martensite island is mostly carried by the laths, which can deform plastically at high stress levels. This behaviour is reflected by the overall response and negligible sliding magnitude of the martensite island in Fig. 4(c–d), showing that the martensite island deforms plastically with very little sliding, at high stress levels. Not surprisingly, high plastic deformation localization occurs in the ferrite matrix around the lath tips (see insets in Fig. 5(b)) as well as around the whole martensite island, while negligible plastic deformation occurs around the RA film tips. Accordingly, the plastic deformation pattern is governed by the interaction between the laths and the ferrite matrix, and correlates with the M/F interfacial morphology. Comparing the results for the unit cells with different interracial morphologies under the same mechanical loading conditions, similar plastic deformation patterns can be found. It can therefore be concluded that the impact of the M/F interfacial morphology is, although present, quite localized and negligible far from the M/F interface.

Next, the M/F interface damage initiation, i.e. potential void nucleation in the near-interface ferrite matrix, is analysed.[1] Since precipitates and ferrite grain boundaries are rarely involved at this scale, only the intra-grain void nucleation mechanism is examined in the following analysis, which physically originates from the dislocation interactions, e.g. relaxation of pile-up of dislocations and annihilation of dislocations gliding along intersecting paths on different planes [65]. Based on this mechanism, the accumulated crystallographic slip has been confirmed [66–68] to be an appropriate damage initiation indicator. Since an isotropic elasto-plastic model is used for the ferrite matrix in this study, the accumulated crystallographic slip is not available. Nevertheless, as stated by Li et al. [69], the equivalent plastic strain is also a suitable measure for the averaged crystallographic micro-slip over all slip systems, comparable to the accumulated crystallographic slip. Hence, the equivalent plastic strain map of the ferrite matrix shown in Fig. 5 is exploited as an indicator for the M/F interface damage initiation. Considering the fact that, as dislocations move, the plastic strain in the near-interface ferrite is largely induced by the martensite island substructure boundary sliding, it can be concluded that the M/F interface damage is initiated by substructure boundary sliding, which is the favourable plastic deformation mode of the martensite islands in DP steels (see also Section 2 and [42,43]). Interestingly, such damage initiation mode is independent of the M/F interfacial morphology(see Fig. 5(a)): all four considered different morphologies induce similar damage initiation patterns. When the substructure boundary sliding is inactive, the interfacial morphology can play an important role and damage initiation can be promoted by the jagged morphology, as shown in Fig. 5(b). The competition between interfacial morphology and substructure boundary sliding is further investigated in Section 4.4.

To check the sensitivity of the damage initiation analysis with respect to the specific choice of the damage initiation indicator, other widely used ductile damage initiation criteria, e.g. those accounting for both plastic deformation and stress triaxiality effects [70,71] or based on the stored energy [72], have also been examined. All considered damage indicators lead to qualitatively similar damage initiation patterns (see Appendix C).

4.2. Influence of the phase contrast

As shown in Table 2, the ferrite matrix properties can vary over a broad range, even for the same carbon content. In order to investigate the influence of the ferrite properties on the M/F interface damage initiation, ferrite matrices softer ($S_0 = 350$ MPa, $S_\infty = 525$ MPa and $E_c = 0.0351$) and harder ($S_0 = 550$ MPa, $S_\infty = 825$ MPa and $E_c = 0.0351$) than the reference value have been considered.

Under simple shear loading, the overall responses of the four unit cell configurations and sliding magnitudes of the martensite islands are reported in Fig. 6, together with the equivalent plastic strain maps in Fig. 7. Note that, irrespective of the change in the F/A phase contrast, the substructure boundary sliding, which is accommodated by the large plastic deformation ($> 40\%$) of RA films, remains strongly active, inducing apparent martensite island plasticity and large plastic deformations in the near-interface ferrite matrix around the RA films. However, comparing with Fig. 4(a–b), the martensite island plasticity and overall sliding are postponed and require a higher stress level to be activated as the F/A phase contrast decreases. By considering Fig. 5(a), this trend can be rationalized as follows. In the case of a softer ferrite matrix, plasticity in the ferrite activates earlier and the substructure boundary sliding activation is thereby delayed. Thus, for the same overall strain, the interaction between the substructure boundary sliding and the ferrite matrix is weaker when the F/A contrast is reduced, resulting in a lower plastic strain magnitude and damage indicator in the near-interface ferrite matrix, which delays the damage initiation, as observed in Fig. 7(a). If instead the F/A contrast is increased, at the same overall strain, the substructure boundary sliding is activated earlier, inducing earlier plastic strain localization, and thus the damage initiation is promoted, as observed in Fig. 7(b).

These numerical investigations agree qualitatively with the experimental observations by Hoefnagels et al. [7], Calcagnotto et al. [73] and Lai et al. [74]. This literature has shown that the M/F interface damage is enhanced by refining the ferrite grains and thus by increasing the hardness of the ferrite matrix. While being in line with our study, these experimental observations presented by Hoefnagels et al. [7], Calcagnotto et al. [73] and Lai et al. [74] contrast with the common understanding predicting less M/F interface damage for an increased ferrite hardness (i.e. lower M/F phase contrast).

Additionally, it can be noticed that the influence of the M/F interfacial morphology is similar to what was observed in Figs. 4(a–b) and 5(a), i.e. it does not change qualitatively with the change in ferrite properties.

To summarize, the simulations reveal that, irrespective of the specific F/A phase contrast, when the load is favourably oriented, substructure boundary sliding occurs and triggers M/F interface damage. The F/A phase contrast determines when this onset of failure will occur: lowering the F/A phase contrast can postpone the activation of the substructure boundary sliding and hence the M/F interface damage initiation as well. This finding is in line with detailed experiments, and contrasts with the common understanding that decreasing the M/F phase contrast helps to avoid M/F interface damage initiation.

4.3. Influence of residual stresses/strains due to the preceding phase transformation

Due to the martensitic phase transformation occurring when DP steels are quenched during processing, considerable residual stress/strain fields may be retained in the as-quenched material. These residual stresses and strains are expected to also affect the M/F interface damage initiation mechanism. It has been shown by Maresca and Curtin [49] that the shape deformation due to the austenite to martensite transformation in low-carbon lath martensite may reach up to $\sim 90\%$ strain, depending on the specific alloy composition. This large shape deformation can induce considerable residual stresses and plastic strains, as shown experimentally in e.g. [75]. In this work, in order to avoid computational issues due to large mesh distortions in the ferrite matrix, relatively smaller ε_{tr} (equal to 20%, $\sim 1\%$ volume expansion) is adopted for the laths. It has been verified that applying higher ε_{tr} (up to 30%) leads to similar qualitative results.

In order to understand the interaction between the substructure boundary sliding mechanism and the different phases during the phase transformation, the residual strain and stress maps induced by the phase transformation are shown in Fig. 8. These values have been used as the initial state preceding all further mechanical loading simulations. The results of the unit cell configurations “IM-2” and “IM-3” are similar to “IM-1” and therefore not shown. Note that the lath stress level is > 2 GPa, namely above its initial yield stress, implying that lath plastic deformation can already take place during the phase transformation, which is consistent with the fact that lath martensite is known to be highly dislocated. This emerges from the constraining effect of the surrounding ferrite matrix on the lath growth. Hydrostatic compressive stress fields are observed in both the laths and the RA films,

[1] Note that the martensite island usually preserves its integrity when the M/F interface damage initiates.

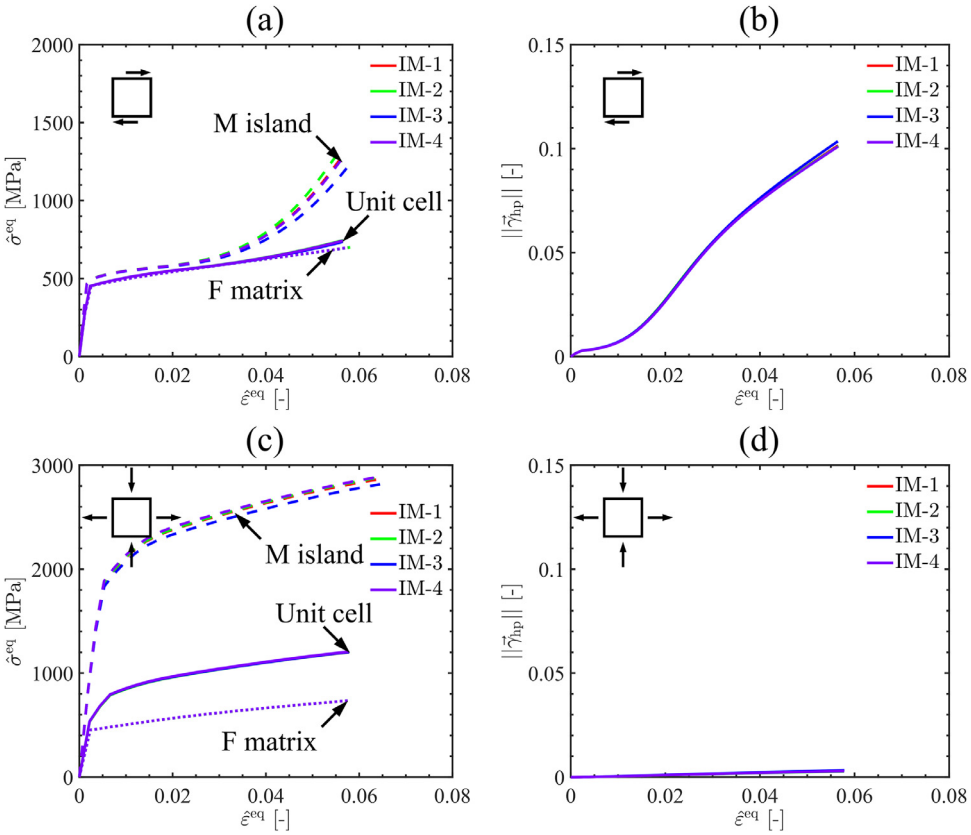

Fig. 4. (a, c) Overall equivalent stress versus strain responses and (b, d) sliding magnitudes (as a function of the equivalent strain) of the corresponding martensite islands for the four unit cell configurations, computed without residual stress/strain effects, under different mechanical loading conditions: (a, b) simple shear and (c, d) biaxial loading. In (a) and (c), the overall responses of the whole unit cell, martensite island inside the unit cell and ferrite matrix inside the unit cell are represented by a solid line, dashed line and dotted line, respectively. (For interpretation of the references to colour in this figure legend, the reader is referred to the web version of this article.)

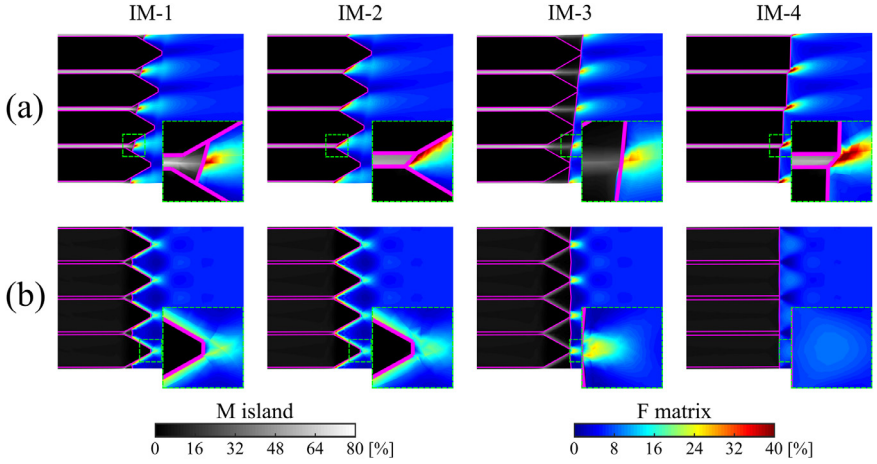

Fig. 5. Equivalent plastic strain maps of the four unit cell configurations, computed without residual stress/strain effects, under different mechanical loading conditions, at a prescribed overall equivalent strain $\hat{\varepsilon}^{eq} = 5.7\%$: (a) simple shear and (b) biaxial loading. Green windows highlight the local magnifications around the RA film tips in (a) and around the lath tips in (b), respectively. Four unit cells are stacked together for better visualization, and only the right near-interface zone is shown. (For interpretation of the references to colour in this figure legend, the reader is referred to the web version of this article.)

which are caused by the volume expansion that occurs during the phase transformation. More interestingly, Fig. 8(c) shows that the substructure boundary sliding already takes place during the phase transformation, opposite to the transformation direction, consistent with the ECCI observations in Fig. 1, which showed sliding laths in the as-quenched DP steel microstructure. Such substructure boundary sliding also induces a residual plastic strain $> 20\%$ and potential damage initiation in the near-interface ferrite matrix. The residual plastic strain maps in the near-interface ferrite matrix in Fig. 8(c) align with the dislocation activity observed in Fig. 1, i.e. plastic deformation is discontinuously along the martensite island boundaries, with a higher intensity at the steps between the laths. However, for the purpose of a direct comparison with experimental measurements, consistent interface structure, material properties and phase transformation strain data is needed, which is not available and therefore beyond the scope of this work.

Next, the results obtained by applying an external mechanical load after the phase transformation ($\varepsilon_{tr} = 20\%$), i.e. accounting

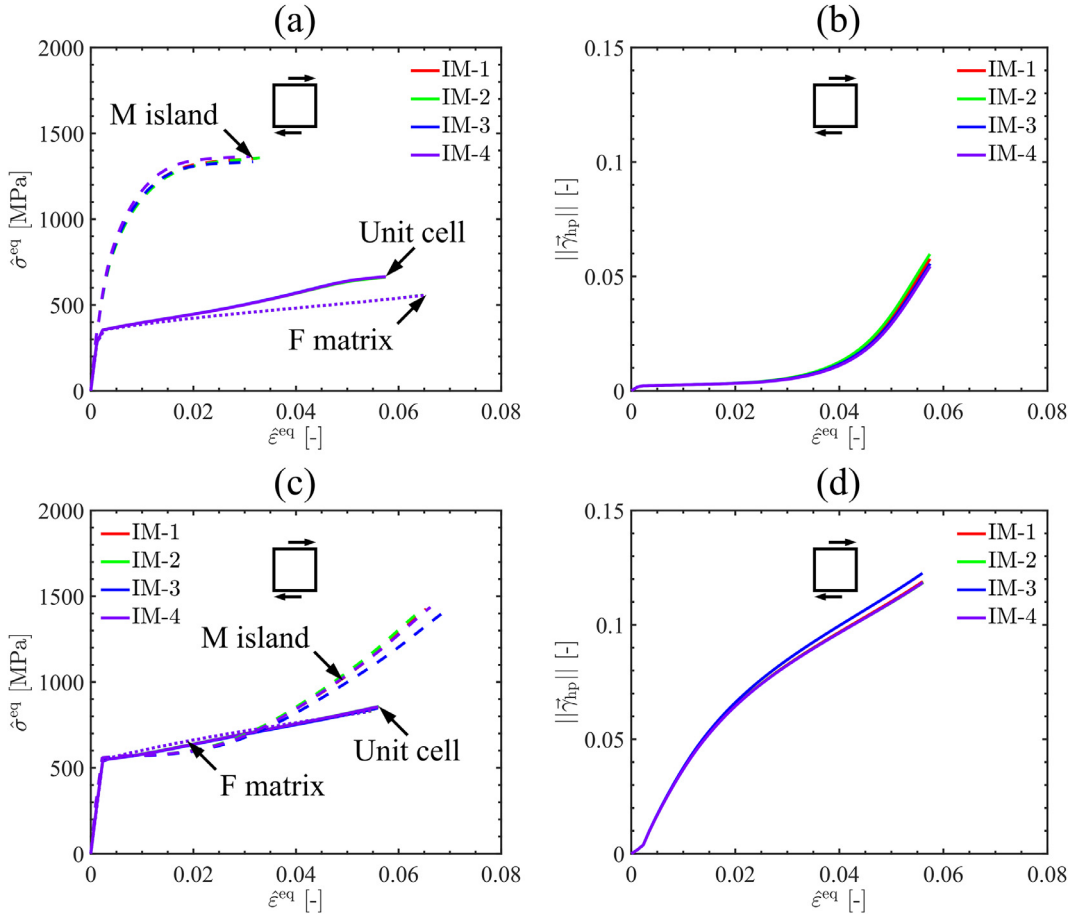

Fig. 6. (a, c) Overall equivalent stress versus strain responses and (b, d) sliding magnitudes (as a function of the equivalent strain) of the corresponding martensite islands for the four unit cell configurations, computed without residual stress/strain effects, under simple shear, for different F/A phase contrasts: (a–b) decreased by ∼ 25%; (c–d) increased by ∼ 25% with respect to the reference value. In (a) and (c), the overall responses of the whole unit cell, martensite island inside the unit cell and ferrite matrix inside the unit cell are represented by a solid line, dashed line and dotted line, respectively. The reference results are shown in Fig. 4(a–b).

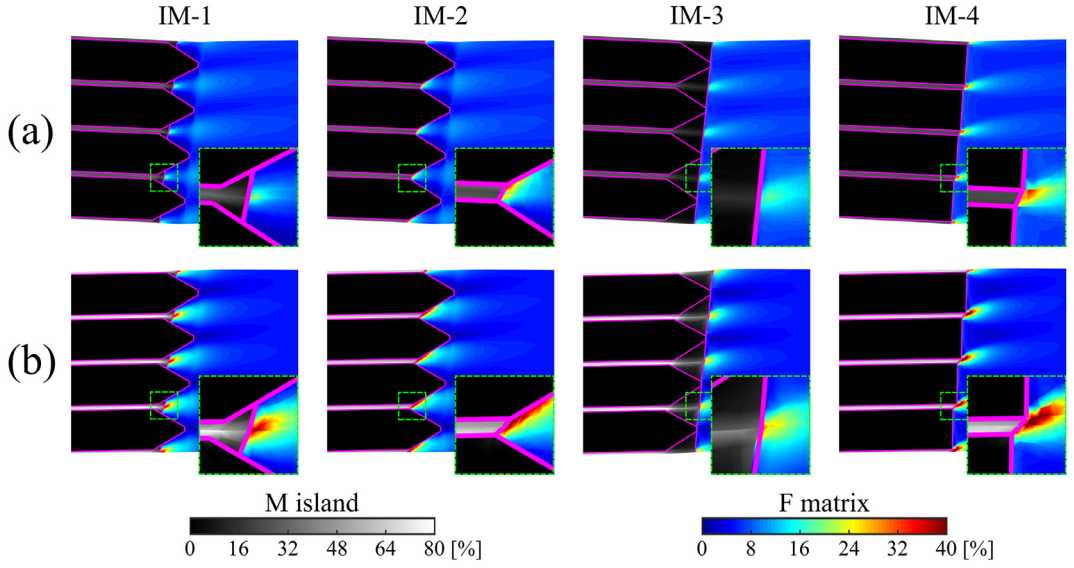

Fig. 7. Equivalent plastic strain maps of the four unit cell configurations, computed without residual stress/strain effects, under simple shear, at a prescribed overall equivalent strain $\hat{\varepsilon}^{eq} = 5.7\%$, for different F/A phase contrasts: (a) decreased by ∼25%; (b) increased by ∼ 25% with respect to the reference value. The reference results are shown in Fig. 5(a).

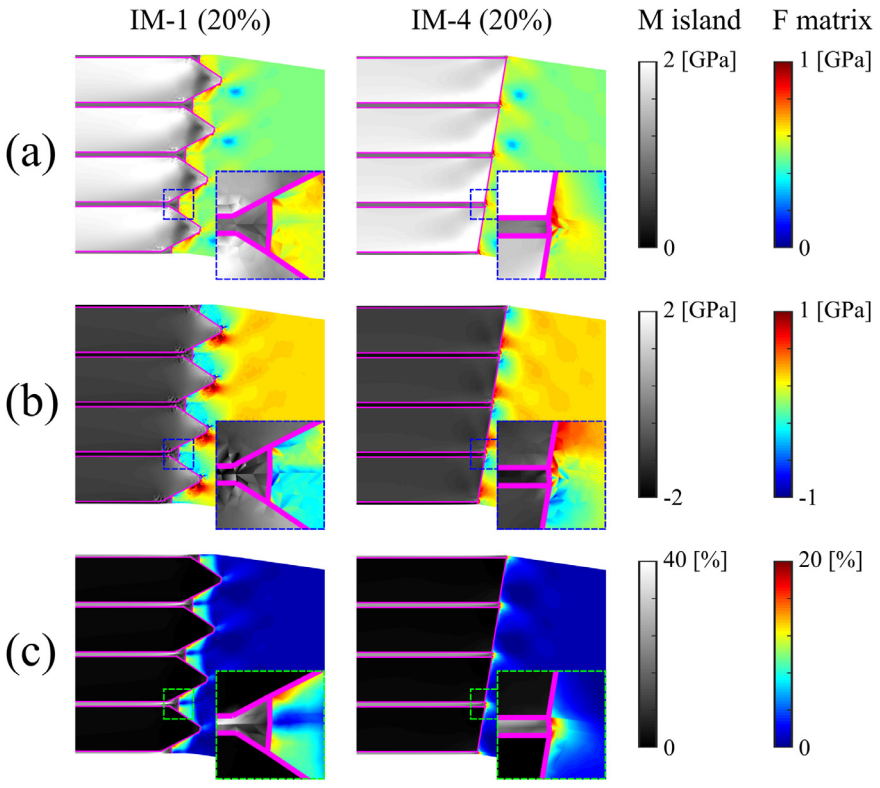

Fig. 8. The response maps of the two unit cell configurations after the phase transformation ($\varepsilon_{tr} = 20\%$), before mechanical loading:(a) equivalent von Mises stress; (b) hydrostatic stress; (c) equivalent plastic strain.

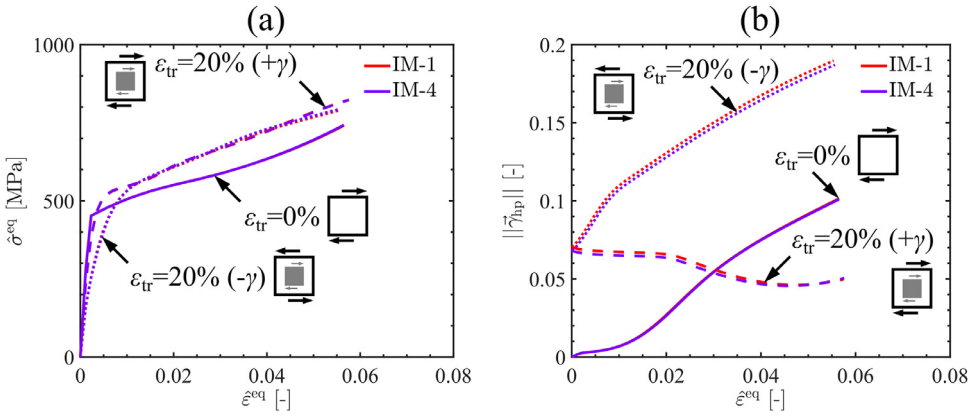

Fig. 9. (a) Overall equivalent stress versus strain responses and (b) sliding magnitudes (as a function of the equivalent strain) of the corresponding martensite islands for the two unit cell configurations, computed without ($\varepsilon_{tr} = 0\%$, in solid line) and with ($\varepsilon_{tr} = 20\%$) the transformation-induced residual stress/strain fields, after subsequent simple shear in two opposite directions: ($+\gamma$, in dashed line) in the direction of the transformation shear (i.e. along the positive X-axis, indicated by the grey arrow) and ($-\gamma$, in dotted line) opposite to the direction of the transformation shear (i.e. along the negative X-axis, indicated by the grey arrow). The sliding contributed by the apparent plasticity of the martensite island during the preceding phase transformation is included in (b), but not the transformation shape change itself. Note that the transformation-induced substructure boundary sliding direction is opposite to the transformation direction (see Fig. 8).

for the transformation-induced stresses/strains, will be compared to the prior results without residual stress/strain effects ($\varepsilon_{tr} = 0\%$). Two simple shear loadings have been considered: the one approximately in the direction as the direction of the transformation shear (i.e. along the positive X-axis), and the other approximately in the direction opposite to the direction of the transformation shear (i.e. along the negative X-axis). Fig. 9 reports, respectively, the overall responses of the two considered unit cell configurations together with the martensite island overall sliding magnitudes. Note, that in Fig. 9(b), the sliding due to the apparent plasticity of the martensite island during the preceding phase transformation is included, while the shearing due to the phase transformation deformation $\mathbf{F}_{tr}$ itself is, instead, subtracted. In Fig. 10, the accumulated (i.e. both during the transformation and the subsequent loading) equivalent plastic strain maps are shown. As can be seen in Fig. 9(a), in absence of residual stresses/strains, the unit cell overall responses under simple shear loading in the two opposite directions are the same due to the symmetry. However, when the residual stresses/strains are induced, the overall responses under mechanical loading differ. When the simple shear direction coincides with the transformation direction, the overall yield stress of the unit cell increases, as a result of the residual stresses and plastic deformation during the phase transformation, leading to the hardening of both the martensite island and the ferrite matrix. Moreover, when

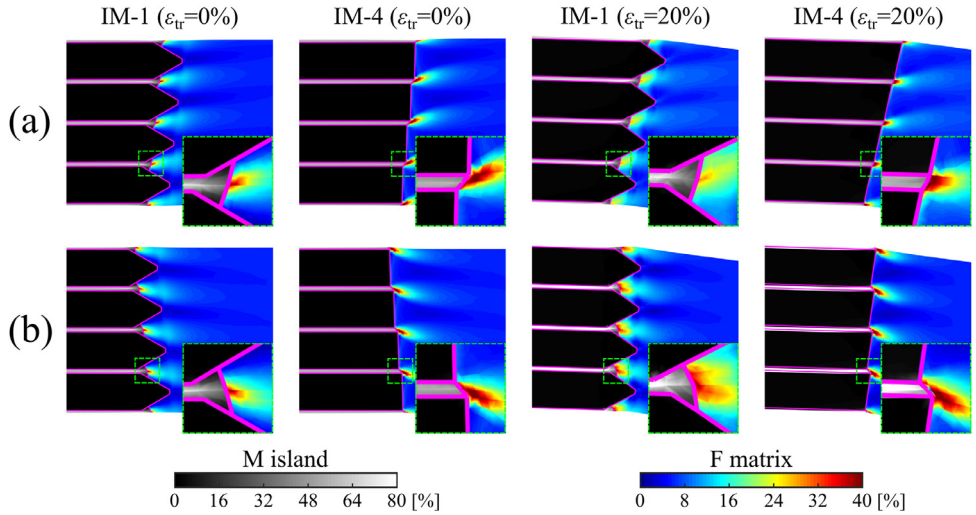

Fig. 10. Equivalent plastic strain maps of the two unit cell configurations, computed without ($\varepsilon_{tr} = 0\%$) and with ($\varepsilon_{tr} = 20\%$) the transformation-induced residual stress/strain fields, after subsequent simple shear in opposite directions: (a) in the direction of the transformation shear (i.e. along the positive X-axis); (b) opposite to the direction of the transformation shear (i.e. along the negative X-axis), at a prescribed overall equivalent strain $\bar{\varepsilon}^{eq} = 5.7\%$. The equivalent plastic strain accumulated during the preceding phase transformation is included.

simple shear loading is applied in the direction of the phase transformation, the sliding magnitude is first decreased and upon further loading it starts to increase again, as shown in Fig. 9(b), because the sliding activated during the phase transformation occurs in the direction opposite to transformation direction. The overall sliding, however, remains pronounced at any applied strain, resulting in an apparent increase of the plastic deformation in both the martensite island and the near-interface ferrite matrix around the RA films, as reported in Fig. 10(a). For simple shear loading in the direction opposite to the phase transformation, further substructure boundary sliding takes place because this occurs in the same direction as the sliding activated during the phase transformation. This larger sliding activity of the martensite island leads to an even larger increase of the plastic deformation in both the martensite island and the near-interface ferrite matrix, as shown in Figs. 9(b) and 10(b). Based on this analysis, it is concluded that the residual stress field can either postpone or promote the M/F interface damage initiation, strongly depending on the subsequent mechanical loading direction relative to the transformation direction, thereby the substructure boundary sliding plays a major role. Although the former conclusion is well established in the literature, the latter, i.e. the role of the substructure boundary sliding, to the best of the authors' knowledge, has not been considered as relevant before. Again, the precise M/F interfacial morphology has a very limited impact even when the residual stresses/strains are accounted for, whereas RA blocks between the lath tips relieve the plastic deformation localization in the near-interface ferrite matrix (see the plastic strain maps of the unit cell configuration "IM-1" in Fig. 10).

These observations show that residual stresses/strains do not impact the M/F interface damage initiation qualitatively, as it remains related to the substructure boundary sliding. However, from a quantitative point of view, the residual stress/strain effects have a significant influence on the M/F interface damage initiation. On the one hand, residual stresses may induce the substructure boundary sliding already before any mechanical load is applied, thus promoting M/F interface damage initiation. On the other hand, depending on the mechanical loading conditions, the accompanying residual stresses can either counteract or increase the substructure boundary sliding activity, thereby postponing or promoting the M/F interface damage initiation. To summarize, the net impact on M/F interface damage initiation can be positive or negative, depending on the competition between the two mentioned effects.

4.4. Competition between substructure boundary sliding and interfacial morphology effects on the M/F interface damage initiation

The results shown so far demonstrate that, when shear is applied parallel to the subgrain lath martensite boundaries, the M/F interface damage initiation is controlled by the substructure boundary sliding of the martensite island. Under different loading conditions, when sliding is not activated, the interfacial morphology may largely affect the damage initiation. The above simulation results presented in Fig. 5 compared different loading cases for the same overall strain magnitude of the M/F interface unit cell. As can be seen from Fig. 4(a) and (c), the martensite island overall strains were also approximately the same for the different loading cases. Therefore, these results do not indicate which mechanism will be prevalent in a DP steel, i.e. whether M/F interface damage initiation will be controlled by the substructure boundary sliding, or by the interfacial morphology effects, or by both mechanisms. As numerically shown by Maresca et al. [42], the deformation behaviour of the martensite islands in the DP steel mesostructure is extremely heterogeneous. At a given *global* stress/strain state, depending on the *local* stress/strain state with respect to the martensite substructure and crystallography, martensite can deform plastically if the substructure boundary sliding is activated, or it undergoes almost purely elastic deformation otherwise. This result qualitatively corresponds to the experimental observations by Ghadbeigi et al. [22,23], who measured very heterogeneous strain distribution of the martensite islands within DP steel microstructures, ranging from 0% up to 110% for an applied tensile strain 42%. Thus, a DP steel can be envisioned as a multi-phase material, in which martensite can behave either as a "hard" phase or as a "soft" phase depending on its orientation and the local stress state. Therefore, using the same value of the martensite island overall strain for comparing different loading cases does not provide a complete picture on the competition between the substructure boundary sliding and interfacial morphology effects with respect to the M/F interface damage initiation. An alternative, possibly more realistic, approach can be to compare different loading cases for the same amount of the overall mechanical work in the martensite island. This approach is similar to the "iso-work" rule of mixtures proposed by Bouaziz and Buessler [76], that has been shown to provide a realistic connection between local and global stress/strain states in multi-phase steels. The two loading cases considered in

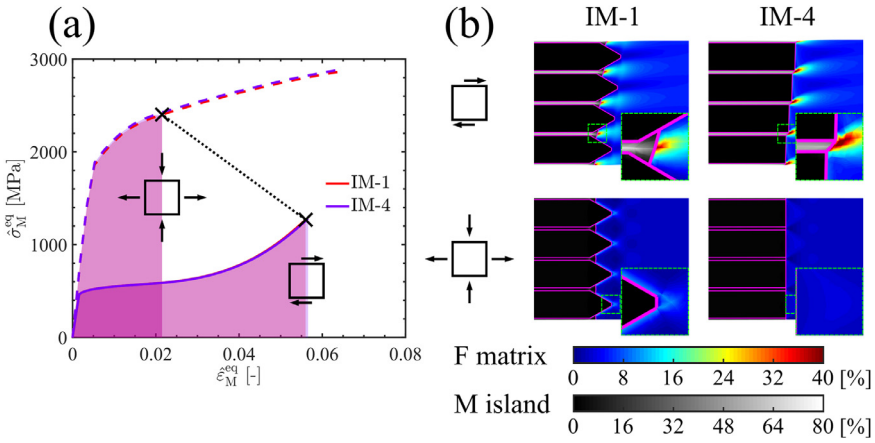

Fig. 11. (a) The simple shear (in solid line) and biaxial loading (in dashed line) cases are compared at the same amount of martensite island overall mechanical work, which is indicated by the area under the overall response curve of the martensite island inside the unit cell; (b) equivalent plastic strain maps of the two unit cell configurations, at the corresponding martensite island stress/strain states indicated by "×" in (a).

this paper are compared at the same amount of martensite island overall mechanical work in Fig. 11. The results of the unit cell configurations "IM-2" and "IM-3" are similar to "IM-1" and are therefore not shown in this comparison.

Fig. 11 reveals that for stress/strain states of the martensite island with the same amount of mechanical work, the damage initiation at the M/F interface will occur much more favourably next to those martensite islands which slide, since they show a significant amount of plastic strain localization. On the other hand, relatively little plastic deformation and hence limited damage will be triggered next to those martensite islands in which the sliding is inactive, even in presence of a jagged M/F interfacial morphology. It can therefore be concluded that in a DP steel, M/F interface damage initiation is dominated by the substructure boundary sliding mechanism.

5. Conclusions

A comprehensive crystal plasticity study has been carried out in order to investigate damage initiation mechanism at M/F interfaces with different morphologies. The main findings are summarized below:

- The M/F interface damage initiation generally originates from the substructure boundary sliding, which is the favourable plastic deformation mode of lath martensite and which can induce high plastic deformation localization in near-interface ferrite matrix in DP steels. Compared with this predominant mechanism, the influences of the M/F interfacial morphology, phase contrast and residual stress/strain effects are small.
- Although the specific interfacial morphology plays a much less important role in the M/F interface damage initiation mechanism, the presence of RA blocks between the lath tips can relieve the plastic deformation localization in the near-interface ferrite matrix.
- Softer ferrite can reduce the activity of substructure boundary sliding, thus postponing the M/F interface damage initiation: this finding contrasts with the common understanding that a harder ferrite (i.e. reduced M/F phase contrast) is beneficial with respect to M/F interface damage initiation, but it is consistent with detailed experimental investigations in the literature [7,73,74].
- The prior phase transformation can already trigger substructure boundary sliding, accompanied by some residual M/F interface damage initiation, even before applying any external mechanical load. The induced residual stress/strain fields may counteract or promote the substructure boundary sliding when mechanical loading is applied, resulting in postponed or promoted M/F interface damage initiation. Due to the competition between these two effects, the phase transformation has a complex net impact on the M/F interface damage initiation.
- Detailed ECCI measurements show the existence of sharp martensite wedges protruding into ferrite, constituting a jagged M/F interface morphology, thereby guiding the modelling choices. As all steps occur at lath boundaries, these observations strengthen the hypothesis of the substructure boundary sliding of martensite islands in DP steels.

This contribution demonstrates the key role of the substructure boundary sliding in triggering M/F interface damage, which paves the way to a novel mechanistic understanding of the origin of M/F interface damage. This finding may offer new guidelines for further product improvements in the steel industry, e.g. by fine tuning and control of the martensite substructure.

The ferrite grain orientation effects and the carbon concentration gradient effects, may become important in particular near the M/F interface. Besides, in a practical DP steel mesostructure, multiple martensite islands exist and thus interactions between different M/F interfaces may occur. Moreover, the fine martensite island can still contain more than one variant and thereby strong interactions among laths belonging to different variants, together with the 3D morphology effects, may also occur, both during the phase transformation and the mechanical loading. These aspects have not been considered here and will be investigated in future work.

Declaration of Competing Interest

The authors declare that they have no known competing financial interests or personal relationships that could have appeared to influence the work reported in this paper.

Acknowledgements

This research was carried out under project number T17019d in the framework of the research program of the Materials Innovation Institute (M2i) (www.m2i.nl) supported by the Dutch government.

Appendix A. Crystal plasticity accounting for phase transformation

The crystal plasticity framework adopted in this work, which incorporates phase transformation, is detailed below. In a finite

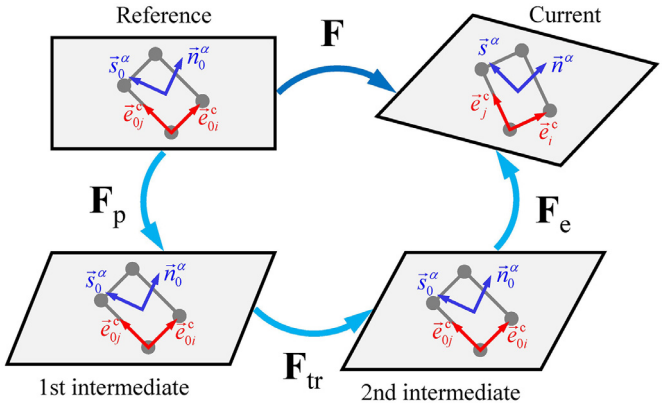

Fig. A.12. Multiplicative decomposition of the total deformation gradient, associated with the reference, first intermediate, second intermediate and current configurations. The phase transformation contributes to the shape change and does not modify the crystal orientation, which is set to be consistent with the OR.

strain setting, the total deformation gradient tensor $\mathbf{F}$ is multiplicatively split into the elastic ($\mathbf{F}_e$), phase transformation ($\mathbf{F}_{tr}$) and plastic ($\mathbf{F}_p$) parts, reading

$$\mathbf{F} = \mathbf{F}_e \cdot \mathbf{F}_{tr} \cdot \mathbf{F}_p, \tag{A.1}$$

where $\mathbf{F}_e$ includes both rotations and elastic strains,$\mathbf{F}_{tr}$ includes the phase transformation shape change and the crystallographic OR between the parent and product phases, while $\mathbf{F}_p$ does not change the crystal orientation. Accordingly, two (fictitious) intermediate stress-free configurations are introduced, as shown in Fig. A.12, where $\vec{e}^c_{0i}$ and $\vec{e}^c_i$ denote the initial and current crystallographic bases of the product phase, and $(\vec{n}^\alpha_0)[\vec{s}^\alpha_0]$ and $(\vec{n}^\alpha)[\vec{s}^\alpha]$ the initial and current slip systems of the product phase, respectively. Note that, for convenience of the implementation, it has been assumed that each product phase variant forms instantaneously. Hence, $\mathbf{F}_{tr}$ can be directly imposed on the whole BCC lath, with its crystal orientation predefined according to the adopted OR model. By using this approach, there is no need to model the parent austenite gain explicitly. Due to the small thickness of the FCC RA film, the whole FCC RA film follows the crystal orientation change of the BCC lath, approximately preserving the predefined OR. In the phase transformation simulation, the induced deviation from the OR has been confirmed to be $\sim 0.5^\circ$, which is indeed negligible.

Elasticity is defined between the second intermediate and the current configurations. It is assumed that the elastic strains of the crystal are small, such that a linear constitutive law is appropriate, reading

$$\bar{\mathbf{S}} = \mathbb{C} : \bar{\mathbf{E}}_e, \tag{A.2}$$

where $\bar{\mathbf{S}} = \mathbf{F}_{tr} \cdot \mathbf{F}_p \cdot \mathbf{S} \cdot \mathbf{F}_p^T \cdot \mathbf{F}_{tr}^T$ denotes the push forward of the second Piola-Kirchhoff stress tensor $\mathbf{S}$ from the reference configuration towards the second intermediate configuration; $\bar{\mathbf{E}}_e = \frac{1}{2}(\bar{\mathbf{C}}_e - \mathbf{I})$ is the elastic Green-Lagrangian strain with $\bar{\mathbf{C}}_e = \mathbf{F}_e^T \cdot \mathbf{F}_e$ and $\mathbf{I}$ the identity tensor. $\mathbb{C}$ is the elasticity tensor that in case of cubic symmetry is identified uniquely by the three elasticity constants C_{11}, C_{12} and C_{44}.

For each martensite variant, $\mathbf{F}_{tr}$ can be generalized as an invariant-plane strain [49]

$$\mathbf{F}_{tr} = \mathbf{I} + \varepsilon_{tr} \vec{s}_{tr} \vec{n}_{hp}, \tag{A.3}$$

where ε_{tr} denotes the transformation strain magnitude, $\vec{s}_{tr}$ the transformation direction and $\vec{n}_{hp}$ the habit plane normal, both defined in the parent FCC crystal coordinate system. Note that $\vec{s}_{tr}$ is generally not perpendicular to $\vec{n}_{hp}$ due to the contribution associated with the volume change. ε_{tr} is determined by the lattice parameter ratio a_{fcc}/a_{bcc} between the parent austenite and product martensite, and thereby the shape change is largely controlled by the carbon content and the other alloying elements.

Plasticity carried by crystallographic slip is defined between the reference and first intermediate configurations. The plastic velocity gradient $\mathbf{L}_p = \dot{\mathbf{F}}_p \cdot \mathbf{F}_p^{-1}$ is computed based on the single slip contributions as

$$\mathbf{L}_p = \sum_{\alpha=1}^{N_s} \dot{\gamma}^\alpha \mathbf{P}_0^\alpha, \tag{A.4}$$

where $\mathbf{P}_0^\alpha = \vec{s}_0^\alpha \vec{n}_0^\alpha$ is the Schmid tensor of the αth slip system in the initial crystal configuration, with $\vec{s}_0^\alpha$ and $\vec{n}_0^\alpha$ are the associated slip direction and slip plane normal, respectively, $\dot{\gamma}^\alpha$ is the plastic slip rate and N_s is the total number of slip systems.

The plastic deformation is governed by the resolved shear stress on each slip system, computed as

$$\tau^\alpha = \bar{\mathbf{S}} \cdot \bar{\mathbf{C}}_e : \mathbf{P}_0^\alpha. \tag{A.5}$$

The model is completed with the expressions for the crystallographic slip γ^α and slip resistance s^α, given in Eqs. (1)–(3). Note that the non-Schmid effects are often added in many BCC crystal studies, to account for the contribution of screw dislocation movement. However, it has been recently shown that the non-Schmid effects are strongly metal-dependent and become negligible for iron-based BCC crystals [77] including ferrite [78], and thus they are not included in the present modelling.

Appendix B. Definition of the overall sliding of the martensite island

In order to conveniently quantify the substructure boundary sliding activity, the overall sliding of the martensite island (assuming a single habit plane) is defined as follows.

Let us denote a fibre through the thickness of the M/A laminate by $\vec{B}$ in the reference configuration, which becomes $\vec{b}$ after deformation, see Fig. B.13 for a 2D simplified illustration, where $\vec{N}_{hp}$ denotes the habit plane normal in the reference configuration, which becomes $\vec{n}_{hp}$ in the deformed configuration. In case of inactive sliding, this fibre simply follows the rotation of the habit

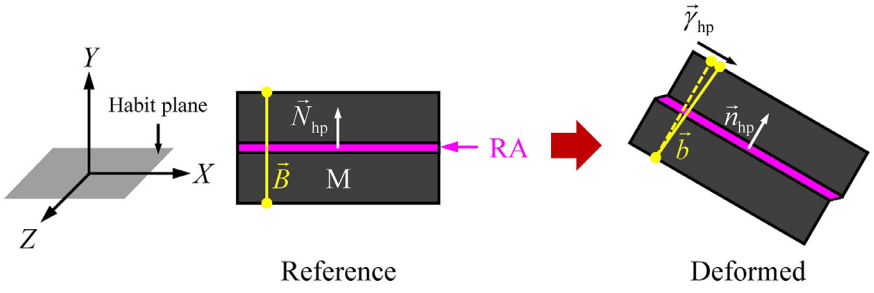

Fig. B.13. Schematic illustration of the overall sliding measure $\vec{\gamma}_{hp}$ of the martensite island during deformation.

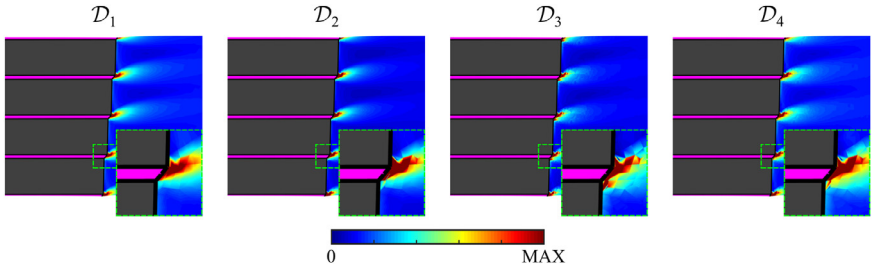

Fig. C.14. Damage initiation maps in the ferrite matrix of the unit cell configuration "IM-4" without residual stress/strain effects, under simple shear, at a prescribed overall equivalent strain $\bar{\varepsilon}^{\mathrm{eq}} = 5.7\%$, using different indicators defined in Eq. (C.1). Colorbar ranges are from 0 to 40% for the equivalent plastic strain-based model, 0 to 16 MJ/m^3 for the stored energy-based model, 0 to 0.2 for the Rice-Tracey model and 0 to 1.6 for the Johnson-Cook model. (For interpretation of the references to colour in this figure legend, the reader is referred to the web version of this article.)

plane, while in case of active sliding (and neglecting the plastic deformation of the laths), additional shear deformation along the habit plane will appear, see Fig. B.13. Therefore, the overall sliding of the martensite island can be defined by tracking the deformation of this fibre and the rotation of the habit plane, as follows

$$\vec{\gamma}_{\mathrm{hp}} = \frac{\vec{b}}{||\vec{B}||} - \vec{n}_{\mathrm{hp}}\left(\vec{n}_{\mathrm{hp}} \cdot \frac{\vec{b}}{||\vec{B}||}\right), \tag{B.1}$$

where $||\vec{B}||$ denotes the fibre length in the reference configuration, and the second term represents the component of $\frac{\vec{b}}{||\vec{B}||}$ perpendicular to the habit plane. The 2D interpretation of $\vec{\gamma}_{\mathrm{hp}}$ is provided in Fig. B.13, showing that $\vec{\gamma}_{\mathrm{hp}}$ is nothing else than the effective shear deformation component of the M/A laminate along the habit plane. Moreover, since active sliding renders the plastic deformation of the laths to be negligible, the defined overall sliding of the martensite island can be used as a measure of the plastic slip activity of the RA films.

Within the FEM framework, $\vec{b}$ and $\vec{n}_{\mathrm{hp}}$ can be approximately determined using the nodal positions, after which $\vec{\gamma}_{\mathrm{hp}}$ can be computed from Eq. (B.1).

Appendix C. Influence of the damage initiation indicator choice

The particular choice of the damage initiation indicator may affect the damage initiation pattern in the ferrite matrix and is therefore examined below. Four different models widely used in the literature are considered, namely

$$\mathcal{D}_1 = \int \dot{\varepsilon}_{\mathrm{p}}^{\mathrm{eq}}\,\mathrm{d}t, \tag{C.1a}$$

$$\mathcal{D}_2 = \int \xi\sigma^{\mathrm{eq}}\dot{\varepsilon}_{\mathrm{p}}^{\mathrm{eq}}\,\mathrm{d}t, \tag{C.1b}$$

$$\mathcal{D}_3 = \int 0.283\exp\left(\frac{3\eta}{2}\right)\dot{\varepsilon}_{\mathrm{p}}^{\mathrm{eq}}\,\mathrm{d}t, \tag{C.1c}$$

$$\mathcal{D}_4 = \int \frac{1}{\varepsilon_{\mathrm{c}}(\eta)}\dot{\varepsilon}_{\mathrm{p}}^{\mathrm{eq}}\,\mathrm{d}t \quad \text{with} \quad \varepsilon_{\mathrm{c}} = \varepsilon_{\mathrm{amp}}\exp\left(-\frac{\eta}{\eta_{\mathrm{e}}}\right) + \varepsilon_0, \tag{C.1d}$$

which refer to the equivalent plastic strain-based model [66–68] (adopted in the main text), stored energy-based model [72], Rice-Tracey model [70] and Johnson-Cook model [71], respectively. Here $\dot{\varepsilon}_{\mathrm{p}}^{\mathrm{eq}} = \sqrt{\frac{2}{3}\dot{\boldsymbol{\varepsilon}}_{\mathrm{p}} : \dot{\boldsymbol{\varepsilon}}_{\mathrm{p}}}$ denotes the equivalent plastic strain rate, σ^{eq} the equivalent von Mises stress, η the stress triaxiality, ξ the stored energy fraction with respect to plastic work, and $\varepsilon_{\mathrm{amp}}$, η_{e} and ε_0 the Johnson-Cook model parameters. In this work, $\xi = 5\%$ is adopted for the stored energy-based model [72] and $\varepsilon_{\mathrm{amp}} = 0.2$, $\eta_{\mathrm{e}} = 0.6$ and $\varepsilon_0 = 0.1$ for the Johnson-Cook model [79], without loss of generality.

In Fig. C.14, the damage initiation maps in the ferrite matrix under simple shear, calculated using different indicators, are compared. As an example, the results for the unit cell configuration "IM-4" without residual stress/strain effects are shown. Clearly, the four indicators lead to remarkably similar damage initiation patterns in the ferrite matrix. It has been verified that this observation also holds for different indicator model parameters, F/A phase contrasts and residual stress/strain due to the preceding phase transformations.

References

[1] N. Lutsey, Review of technical literature and trends related to automobile mass-reduction technology, Technical Report, University of California, Davis, 2010. UCD-ITS-RR-10-10
[2] M. Mazinani, W. Poole, Effect of martensite plasticity on the deformation behavior of a low-carbon dual-phase steel, Metall. Mater. Trans. A 38 (2) (2007) 328–339, doi:10.1007/s11661-006-9023-3.
[3] A. Pierman, O. Bouaziz, T. Pardoen, P. Jacques, L. Brassart, The influence of microstructure and composition on the plastic behaviour of dual-phase steels, Acta Mater. 73 (2014) 298–311, doi:10.1016/j.actamat.2014.04.015.
[4] S. Sun, M. Pugh, Properties of thermomechanically processed dual-phase steels containing fibrous martensite, Mater. Sci. Eng. A 335 (1–2) (2002) 298–308, doi:10.1016/S0921-5093(01)01942-6.
[5] M. Calcagnotto, D. Ponge, D. Raabe, Effect of grain refinement to 1 µm on strength and toughness of dual-phase steels, Mater. Sci. Eng. A 527 (29–30) (2010) 7832–7840, doi:10.1016/j.msea.2010.08.062.
[6] C. Tasan, M. Diehl, D. Yan, M. Bechtold, F. Roters, L. Schemmann, C. Zheng, N. Peranio, D. Ponge, M. Koyama, K. Tsuzaki, D. Raabe, An overview of dual-phase steels: advances in microstructure-oriented processing and micromechanically guided design, Annu. Rev. Mater. Res. 45 (1) (2015) 391–431, doi:10.1146/annurev-matsci-070214-021103.
[7] J. Hoefnagels, C. Tasan, F. Maresca, F. Peters, V. Kouznetsova, Retardation of plastic instability via damage-enabled microstrain delocalization, J. Mater. Sci. 50 (21) (2015) 6882–6897, doi:10.1007/s10853-015-9164-0.
[8] E. Maire, O. Bouaziz, M. Di Michiel, C. Verdu, Initiation and growth of damage in a dual-phase steel observed by X-ray microtomography, Acta Mater. 56 (18) (2008) 4954–4964, doi:10.1016/j.actamat.2008.06.015.
[9] K. Isik, G. Gerstein, T. Clausmeyer, F. Nürnberger, A.E. Tekkaya, H. Maier, Evaluation of void nucleation and development during plastic deformation of dual-phase steel DP600, Steel Res. Int. 87 (12) (2016) 1583–1591, doi:10.1002/srin.201500483.
[10] N. Saeidi, F. Ashrafizadeh, B. Niroumand, F. Barlat, EBSD study of damage mechanisms in a high-strength ferrite-martensite dual-phase steel, J. Mater. Eng. Perform. 24 (1) (2015) 53–58, doi:10.1007/s11665-014-1257-4.
[11] A. Stroh, A theoretical calculation of the stored energy in a work-hardened material, Proc. R. Soc. Lond. Ser. A 218 (1134) (1953) 391–400, doi:10.1098/rspa.1953.0112.
[12] A. Stroh, The formation of cracks as a result of plastic flow, Proc. R. Soc. Lond. Ser. A 223 (1154) (1954) 404–414, doi:10.1098/rspa.1954.0124.
[13] N. Saeidi, F. Ashrafizadeh, B. Niroumand, F. Barlat, Evaluation of fracture micromechanisms in a fine-grained dual phase steel during uniaxial tensile deformation, Steel Res. Int. 85 (9) (2014) 1386–1392, doi:10.1002/srin.201300344.
[14] D. Das, P. Chattopadhyay, Influence of martensite morphology on the work-hardening behavior of high strength ferrite–martensite dual-phase steel, J. Mater. Sci. 44 (11) (2009) 2957–2965, doi:10.1007/s10853-009-3392-0.
[15] J. Kadkhodapour, A. Butz, S. Ziaei Rad, Mechanisms of void formation during tensile testing in a commercial, dual-phase steel, Acta Mater. 59 (7) (2011) 2575–2588, doi:10.1016/j.actamat.2010.12.039.
[16] G. Avramovic-Cingara, Y. Ososkov, M. Jain, D. Wilkinson, Effect of martensite distribution on damage behaviour in DP600 dual phase steels, Mater. Sci. Eng. A 516 (1–2) (2009) 7–16, doi:10.1016/j.msea.2009.03.055.

[17] F. Archie, X. Li, S. Zaefferer, Micro-damage initiation in ferrite-martensite DP microstructures: a statistical characterization of crystallographic and chemical parameters, Mater. Sci. Eng. A 701 (2017) 302–313, doi:10.1016/j.msea.2017.06.094.

[18] H. Hosseini-Toudeshky, B. Anbarlooie, J. Kadkhodapour, Micromechanics stress–strain behavior prediction of dual phase steel considering plasticity and grain boundaries debonding, Mater. Des. 68 (2015) 167–176, doi:10.1016/j.matdes.2014.12.013.

[19] T. Matsuno, C. Teodosiu, D. Maeda, A. Uenishi, Mesoscale simulation of the early evolution of ductile fracture in dual-phase steels, Int. J. Plast. 74 (2015) 17–34, doi:10.1016/j.ijplas.2015.06.004.

[20] D. Kim, E. Kim, J. Han, W. Woo, S. Choi, Effect of microstructural factors on void formation by ferrite/martensite interface decohesion in DP980 steel under uniaxial tension, Int. J. Plast. 94 (2017) 3–23, doi:10.1016/j.ijplas.2017.04.019.

[21] J. Kang, Y. Ososkov, J. Embury, D. Wilkinson, Digital image correlation studies for microscopic strain distribution and damage in dual phase steels, Scr. Mater. 56 (11) (2007) 999–1002, doi:10.1016/j.scriptamat.2007.01.031.

[22] H. Ghadbeigi, C. Pinna, S. Celotto, J. Yates, Local plastic strain evolution in a high strength dual-phase steel, Mater. Sci. Eng. A 527 (18–19) (2010) 5026–5032, doi:10.1016/j.msea.2010.04.052.

[23] H. Ghadbeigi, C. Pinna, S. Celotto, Failure mechanisms in DP600 steel: initiation, evolution and fracture, Mater. Sci. Eng. A 588 (2013) 420–431, doi:10.1016/j.msea.2013.09.048.

[24] Q. Han, Y. Kang, P. Hodgson, N. Stanford, Quantitative measurement of strain partitioning and slip systems in a dual-phase steel, Scr. Mater. 69 (1) (2013) 13–16, doi:10.1016/j.scriptamat.2013.03.021.

[25] K. Park, M. Nishiyama, N. Nakada, T. Tsuchiyama, S. Takaki, Effect of the martensite distribution on the strain hardening and ductile fracture behaviors in dual-phase steel, Mater. Sci. Eng. A 604 (2014) 135–141, doi:10.1016/j.msea.2014.02.058.

[26] N. Kamikawa, M. Hirohashi, Y. Sato, E. Chandiran, G. Miyamoto, T. Furuhara, Tensile behavior of ferrite-martensite dual phase steels with nano-precipitation of vanadium carbides, ISIJ Int. 55 (8) (2015) 1781–1790, doi:10.2355/isijinternational.ISIJINT-2015-106.

[27] J. Samei, D. Green, S. Golovashchenko, Metallurgical investigations on hyperplasticity in dual phase steel sheets, J. Manuf. Sci. Eng. 136 (4) (2014), doi:10.1115/1.4027492.

[28] G. Krauss, Martensite in steel: strength and structure, Mater. Sci. Eng. A 273-275 (1999) 40–57, doi:10.1016/S0921-5093(99)00288-9.

[29] S. Morito, H. Tanaka, R. Konishi, T. Furuhara, T. Maki, The morphology and crystallography of lath martensite in Fe-C alloys, Acta Mater. 51 (6) (2003) 1789–1799, doi:10.1016/S1359-6454(02)00577-3.

[30] S. Morito, X. Huang, T. Furuhara, T. Maki, N. Hansen, The morphology and crystallography of lath martensite in alloy steels, Acta Mater. 54 (19) (2006) 5323–5331, doi:10.1016/j.actamat.2006.07.009.

[31] C. Du, J. Hoefnagels, R. Vaes, M. Geers, Plasticity of lath martensite by sliding of substructure boundaries, Scr. Mater. 120 (2016) 37–40, doi:10.1016/j.scriptamat.2016.04.006.

[32] J. Inoue, A. Sadeghi, T. Koseki, Slip band formation at free surface of lath martensite in low carbon steel, Acta Mater. 165 (2019) 129–141, doi:10.1016/j.actamat.2018.11.026.

[33] B. Sandvik, C. Wayman, Crystallography and substructure of lath martensite formed in carbon steels, Metallography 16 (2) (1983) 199–227, doi:10.1016/0026-0800(83)90005-8.

[34] P. Kelly, A. Jostsons, R. Blake, The orientation relationship between lath martensite and austenite in low carbon, low alloy steels, Acta Metall. Mater. 38 (6) (1990) 1075–1081, doi:10.1016/0956-7151(90)90180-O.

[35] S. Morito, K. Oh-ishi, K. Hono, T. Ohba, Carbon enrichment in retained austenite films in low carbon lath martensite steel, ISIJ Int. 51 (7) (2011) 1200–1202, doi:10.2355/isijinternational.51.1200.

[36] X. Liao, X. Wang, Z. Guo, M. Wang, Y. Wu, Y. Rong, Microstructures in a resistance spot welded high strength dual phase steel, Mater. Charact. 61 (3) (2010) 341–346, doi:10.1016/j.matchar.2009.12.018.

[37] H. Yoshida, S. Takagi, S. Sakai, S. Morito, T. Ohba, Crystallographic analysis of lath martensite in ferrite-martensite dual phase steel sheet annealed after cold-rolling, ISIJ Int. 55 (10) (2015) 2198–2205, doi:10.2355/isijinternational.ISIJINT-2014-641.

[38] F. Maresca, V. Kouznetsova, M. Geers, On the role of interlath retained austenite in the deformation of lath martensite, Model. Simul. Mater. Sci. Eng. 22 (4) (2014) 045011, doi:10.1088/0965-0393/22/4/045011.

[39] F. Maresca, V. Kouznetsova, M. Geers, Subgrain lath martensite mechanics: a numerical-experimental analysis, J. Mech. Phys. Solids 73 (2014) 69–83, doi:10.1016/j.jmps.2014.09.002.

[40] F. Maresca, V. Kouznetsova, M. Geers, W. Curtin, Contribution of austenite-martensite transformation to deformability of advanced high strength steels: From atomistic mechanisms to microstructural response, Acta Mater. 156 (2018) 463–478, doi:10.1016/j.actamat.2018.06.028.

[41] B. Chehab, X. Wang, J.-P. Masse, O. Bouaziz, H. Zurob, D. Embury, Bulk nanoscale materials in steel products, J. Phys. Conf. Ser. 240 (2010) 012135, doi:10.1088/1742-6596/240/1/012135.

[42] F. Maresca, V. Kouznetsova, M. Geers, Deformation behaviour of lath martensite in multi-phase steels, Scr. Mater. 110 (2016) 74–77, doi:10.1016/j.scriptamat.2015.08.004.

[43] C. Du, R. Petrov, M. Geers, J. Hoefnagels, Lath martensite plasticity enabled by apparent sliding of substructure boundaries, Mater. Des. 172 (2019) 107646, doi:10.1016/j.matdes.2019.107646.

[44] J. Liu, C. Chen, Q. Feng, X. Fang, H. Wang, F. Liu, J. Lu, D. Raabe, Dislocation activities at the martensite phase transformation interface in metastable austenitic stainless steel: an in-situ TEM study, Mater. Sci. Eng. A 703 (2017) 236–243, doi:10.1016/j.msea.2017.06.107.

[45] D. Ping, S. Guo, M. Imura, X. Liu, T. Ohmura, M. Ohnuma, X. Lu, T. Abe, H. Onodera, Lath formation mechanisms and twinning as lath martensite substructures in an ultra low-carbon iron alloy, Sci. Rep. 8 (1) (2018) 14264, doi:10.1038/s41598-018-32679-6.

[46] S. Zaefferer, N. Elhami, Theory and application of electron channelling contrast imaging under controlled diffraction conditions, Acta Mater. 75 (2014) 20–50, doi:10.1016/j.actamat.2014.04.018.

[47] C. Du, J. Hoefnagels, S. Kölling, M. Geers, J. Sietsma, R. Petrov, V. Bliznuk, P. Koenraad, D. Schryvers, B. Amin-Ahmadi, Martensite crystallography and chemistry in dual phase and fully martensitic steels, Mater. Charact. 139 (2018) 411–420, doi:10.1016/j.matchar.2018.03.011.

[48] G. Krauss, A. Marder, The morphology of martensite in iron alloys, Metall. Trans. 2 (9) (1971) 2343–2357, doi:10.1007/BF02814873.

[49] F. Maresca, W. Curtin, The austenite/lath martensite interface in steels: structure, athermal motion, and in-situ transformation strain revealed by simulation and theory, Acta Mater. 134 (2017) 302–323, doi:10.1016/j.actamat.2017.05.044.

[50] V. Kouznetsova, W. Brekelmans, F. Baaijens, An approach to micro-macro modeling of heterogeneous materials, Comput. Mech. 27 (1) (2001) 37–48, doi:10.1007/s004660000212.

[51] S. Kalidindi, C. Bronkhorst, L. Anand, Crystallographic texture evolution in bulk deformation processing of FCC metals, J. Mech. Phys. Solids 40 (3) (1992) 537–569, doi:10.1016/0022-5096(92)80003-9.

[52] J. Hutchinson, Bounds and self-consistent estimates for creep of polycrystalline materials, Proc. R. Soc. A 348 (1652) (1976) 101–127, doi:10.1098/rspa.1976.0027.

[53] T. Wu, J.L. Bassani, C. Laird, Latent hardening in single crystals I: theory and experiments, Proc. R. Soc. A 435 (1893) (1991) 1–19, doi:10.1098/rspa.1991.0127.

[54] Y. Mine, K. Hirashita, H. Takashima, M. Matsuda, K. Takashima, Micro-tension behaviour of lath martensite structures of carbon steel, Mater. Sci. Eng. A 560 (2013) 535–544, doi:10.1016/j.msea.2012.09.099.

[55] T. Niino, J. Inoue, M. Ojima, S. Nambu, T. Koseki, Effects of solute carbon on the work hardening behavior of lath martensite in low-carbon steel, ISIJ Int. 57 (1) (2017) 181–188, doi:10.2355/isijinternational.ISIJINT-2016-430.

[56] H. Bhadeshia, R. Honeycombe, Steels: Microstructure and Properties, Elsevier, Oxford, 2006.

[57] H. Ghassemi-Armaki, R. Maaß, S. Bhat, S. Sriram, J. Greer, K. Kumar, Deformation response of ferrite and martensite in a dual-phase steel, Acta Mater. 62 (2014) 197–211, doi:10.1016/j.actamat.2013.10.001.

[58] C. Tian, D. Ponge, L. Christiansen, C. Kirchlechner, On the mechanical heterogeneity in dual phase steel grades: activation of slip systems and deformation of martensite in DP800, Acta Mater. 183 (2020) 274–284, doi:10.1016/j.actamat.2019.11.002.

[59] J. Rosenberg, H. Piehler, Calculation of the taylor factor and lattice rotations for BCC metals deforming by pencil glide, Metall. Trans. 2 (1) (1971) 257–259, doi:10.1007/BF02662666.

[60] T. de Geus, F. Maresca, R. Peerlings, M. Geers, Microscopic plasticity and damage in two-phase steels: on the competing role of crystallography and phase contrast, Mech. Mater. 101 (2016) 147–159, doi:10.1016/j.mechmat.2016.07.014.

[61] T. Matsuno, R. Ando, N. Yamashita, H. Yokota, K. Goto, I. Watanabe, Analysis of preliminary local hardening close to the ferrite-martensite interface in dual-phase steel by a combination of finite element simulation and nanoindentation test, Int. J. Mech. Sci. 180 (2020) 105663, doi:10.1016/j.ijmecsci.2020.105663.

[62] S. Brown, K. Kim, L. Anand, An internal variable constitutive model for hot working of metals, Int. J. Plast. 5 (2) (1989) 95–130, doi:10.1016/0749-6419(89)90025-9.

[63] F. Lani, Q. Furnémont, T. Van Rompaey, F. Delannay, P. Jacques, T. Pardoen, Multiscale mechanics of TRIP-assisted multiphase steels: II. Micromechanical modelling, Acta Mater. 55 (11) (2007) 3695–3705, doi:10.1016/j.actamat.2007.02.015.

[64] Z. Tao, K. Rasmussen, Stress-strain model for ferritic stainless steels, J. Mater. Civ. Eng. 28 (2) (2016) 06015009, doi:10.1061/(ASCE)MT.1943-5533.0001393.

[65] O. Furukimi, C. Kiattisaksri, Y. Takeda, M. Aramaki, S. Oue, S. Munetoh, M. Tanaka, Void nucleation behavior of single-crystal high-purity iron specimens subjected to tensile deformation, Mater. Sci. Eng. A 701 (2017) 221–225, doi:10.1016/j.msea.2017.06.084.

[66] K. Cheong, M. Smillie, D. Knowles, Predicting fatigue crack initiation through image-based micromechanical modeling, Acta Mater. 55 (5) (2007) 1757–1768, doi:10.1016/j.actamat.2006.10.038.

[67] F. Dunne, A. Wilkinson, R. Allen, Experimental and computational studies of low cycle fatigue crack nucleation in a polycrystal, Int. J. Plast. 23 (2) (2007) 273–295, doi:10.1016/j.ijplas.2006.07.001.

[68] C. Sweeney, W. Vorster, S. Leen, E. Sakurada, P. McHugh, F. Dunne, The role of elastic anisotropy, length scale and crystallographic slip in fatigue crack nucleation, J. Mech. Phys. Solids 61 (5) (2013) 1224–1240, doi:10.1016/j.jmps.2013.01.001.

[69] D. Li, R. Barrett, P. O'Donoghue, N. O'Dowd, S. Leen, A multi-scale crystal plasticity model for cyclic plasticity and low-cycle fatigue in a precipitate-strengthened steel at elevated temperature, J. Mech. Phys. Solids 101 (2017) 44–62, doi:10.1016/j.jmps.2016.12.010.

[70] J. Rice, D. Tracey, On the ductile enlargement of voids in triaxial stress fields, J. Mech. Phys. Solids 17 (3) (1969) 201–217, doi:10.1016/0022-5096(69)90033-7.
[71] G. Johnson, W. Cook, Fracture characteristics of three metals subjected to various strains, strain rates, temperatures and pressures, Eng. Fract. Mech. 21 (1) (1985) 31–48, doi:10.1016/0013-7944(85)90052-9.
[72] V. Wan, D. MacLachlan, F. Dunne, A stored energy criterion for fatigue crack nucleation in polycrystals, Int. J. Fatigue 68 (2014) 90–102, doi:10.1016/j.ijfatigue.2014.06.001.
[73] M. Calcagnotto, Y. Adachi, D. Ponge, D. Raabe, Deformation and fracture mechanisms in fine- and ultrafine-grained ferrite/martensite dual-phase steels and the effect of aging, Acta Mater. 59 (2) (2011) 658–670, doi:10.1016/j.actamat.2010.10.002.
[74] Q. Lai, O. Bouaziz, M. Gouné, A. Perlade, Y. Bréchet, T. Pardoen, Microstructure refinement of dual-phase steels with 3.5 wt% Mn: influence on plastic and fracture behavior, Mater. Sci. Eng. A 638 (2015) 78–89, doi:10.1016/j.msea.2015.04.044.
[75] G. Miyamoto, A. Shibata, T. Maki, T. Furuhara, Precise measurement of strain accommodation in austenite matrix surrounding martensite in ferrous alloys by electron backscatter diffraction analysis, Acta Mater. 57 (4) (2009) 1120–1131, doi:10.1016/j.actamat.2008.10.050.
[76] O. Bouaziz, P. Buessler, Iso-work increment assumption for heterogeneous material behaviour modelling, Adv. Eng. Mater. 6 (12) (2004) 79–83, doi:10.1002/adem.200300524.
[77] L. Dezerald, D. Rodney, E. Clouet, L. Ventelon, F. Willaime, Plastic anisotropy and dislocation trajectory in BCC metals, Nat. Commun. 7 (1) (2016) 11695, doi:10.1038/ncomms11695.
[78] C. Du, F. Maresca, M. Geers, J. Hoefnagels, Ferrite slip system activation investigated by uniaxial micro-tensile tests and simulations, Acta Mater. 146 (2018) 314–327, doi:10.1016/j.actamat.2017.12.054.
[79] N. Vajragupta, V. Uthaisangsuk, B. Schmaling, S. Münstermann, A. Hartmaier, W. Bleck, A micromechanical damage simulation of dual phase steels using XFEM, Comput. Mater. Sci. 54 (2012) 271–279, doi:10.1016/j.commatsci.2011.10.035.